Research Square

Preprints are preliminary reports that have not undergone peer review.
They should not be considered conclusive, used to inform clinical practice,
or referenced by the media as validated information.

Magnetohydrodynamic Analysis of Unsteady Williamson Nanofluid Flow over a Permeable Inclined Stretching Sheet with Cattaneo-Christov Double-Diffusion Effects

Berihun Gizachew Negash

berihungizachew2008@gmail.com

Bahir Dar University

Hunegnaw Dessie

Bahir Dar Univesity

Eshetu Haile

Bahir Dar University

Tadesse Walelign

Debre Tabor University

Research Article

Keywords: Unsteady flow, Williamson nanofluid, inclined stretching sheet, Porous medium, Dufour-Soret effects, inclined magnetic field, OHAM, Cattaneo–Christov model

Posted Date: April 15th, 2026

DOI: https://doi.org/10.21203/rs.3.rs-9411000/v1

License: This work is licensed under a Creative Commons Attribution 4.0 International License.
Read Full License

Additional Declarations: The authors declare no competing interests.

Magnetohydrodynamic Analysis of Unsteady Williamson Nanofluid Flow over a Permeable Inclined Stretching Sheet with Cattaneo-Christov Double-Diffusion Effects

Berihun Gizachew[1*], Hunegnaw Dessie[2], Eshetu Haile[3], Tadesse Walelign[4]

[1,2,3] Department of Mathematics, College of Science, Bahir Dar University, P.O. Box 79, Bahir Dar, Ethiopia.

[4] Department of Mathematics, College of Natural & Computational Sciences, Debre Tabor University, P.O. Box 272, Debre Tabor, Ethiopia

Emails: [1]berihungizachew2008@gmail.com, [2]hunegnawd@yahoo.com, [3]eshetuhg@gmail.com, [4] tadelenyosy@gmail.com

Abstract

This paper investigates the unsteady magnetohydrodynamic (MHD) flow of a Williamson nanofluid across a permeable stretching inclined sheet. The work is intended to fill the information gap regarding the simultaneous effects of unsteadiness, inclined sheet/magnetic field geometry, cross-diffusion, Joule heating, thermal radiation, chemical reaction, heat source/sink and suction/injection under non-Fourier and non-Fick transport models in a porous medium. The governing PDEs undergo similarity transformations to produce a system of coupled nonlinear ODEs. The resulting boundary value problem is addressed semi-analytically using the optimal homotopy analysis method (OHAM). The skin friction coefficient, Nusselt number, Sherwood number, velocity, temperature and concentration profiles are analyzed numerically and graphically in relation to significant dimensionless parameters. Results show that fluid velocity is significantly suppressed by the magnetic field and unsteadiness parameters because of the resistive Lorentz force. The skin-friction coefficient increases by about 29.6% when the magnetic parameter is increased from 0.3 to 1.0. When it comes to thermal transport, the Nusselt number drops by around 44% as the Brownian motion parameter increases from 0.1 to 0.7, but geometric optimization performs well; the heat transfer rate is increased by about 26% when the sheet's inclination angle is reduced from $\pi/6$ to $\pi/12$. Additionally, when the thermal radiation parameter is increased from 0.1 to 0.7, the mass transfer rate shows a significant rise of nearly 68%. This study reveals that the Cattaneo-Christov model offers a more realistic representation of transport mechanisms in viscoelastic nanofluids than classical Fourier and Fick laws, providing important insights for improving conductive nanofluid processing and electromagnetic casting.

Keywords: Unsteady flow, Williamson nanofluid, inclined stretching sheet, Porous medium, Dufour-Soret effects, inclined magnetic field, OHAM, Cattaneo–Christov model

Nomenclatures

x, y Cartesian coordinates (m)

t Time (s)

u, v Velocity components in the x and y directions $(m.s^{-1})$

f Dimensionless stream function

T Temperature (K)

C Fluid concentration $(Kg.m^{-3})$

U Stretching velocity of the sheet $(m.s^{-1})$

a, d Positive constants related to linear stretching (s^{-1})

V Suction/injection velocity scale $(m.s^{-1})$

c_p Specific heat capacity at constant pressure $(J.Kg^{-1}.K^{-1})$

K_0 Permeability of porous medium (m^2)

B_0 Applied magnetic field (Tesla)

$B(t)$ Time-dependent magnetic field (Tesla)

g Gravitational acceleration $(m.s^{-2})$

D_B Brownian diffusion coefficient $(m^2.s^{-1})$

D_T Thermophoretic diffusion coefficient $(m^2.s^{-1})$

D_m Molecular diffusion coefficient $(m^2.s^{-1})$

$\not{k}$ Thermal absorption coefficient (radiation) (m^{-1})

k Thermal conductivity (W. $m^{-1}.K^{-1}$)

Q_0 Heat source/sink coefficient $(J.s^{-1}.m^{-3})$

$\mathbb{k}$ Diffusion ratio

Cs Concentration susceptibility $(Kg.m^{-5}.s^2)$

q Heat flux $(W.m^{-2})$

$\boldsymbol{S}$ Cauchy stress tensor $(Kg.m^{-1}.s^{-2})$

Kr Chemical reaction rate (s^{-1})

P Pressure $(Kg.m^{-1}.s^{-2})$

I Identity tensor

$\mathbb{A}_1$ First Rivlin-Ericksen tensor or Strain rate tensor (s^{-1})

Cf Skin friction coefficient

Nu Nusselt number

Sh Sherwood number

We Weissenberg number

M Magnetic parameter

S Suction/injection parameter

Ec Eckert number

Sc Schmidt number

Re Reynolds number

Rd Thermal radiation parameter

A Unsteadiness parameter

Kp Porosity parameter

Gr Grashof number

Nb Brownian motion parameter

Nt Thermophoresis parameter

JH Joule heating parameter

Du Dufour number

$\mathbb{Q}$ Heat source parameter

Sr Soret number

Pr Prandtl number

Greek symbols

ψ Stream function $(m^2.s^{-1})$

η Similarity variable

θ Dimensionless temperature

ϕ Dimensionless concentration

γ Chemical reaction parameter

ρ Fluid density $(Kg.m^{-3})$

μ Dynamic viscosity $(Kg.m^{-1}.s^{-1})$

υ Kinematic viscosity $(m^2.s^{-1})$

$\boldsymbol{\sigma}$ Electrical conductivity of the fluid ($S.m^{-1}$ - Siemens per meter)

β_T Thermal volumetric expansion coefficient (K^{-1})

β_C Solutal volumetric expansion coefficient $(Kg^{-1}.m^3)$

α Thermal diffusivity of the fluid $(m^2.s^{-1})$

τ Ratio of nanoparticle heat capacity to base fluid heat capacity

σ Stefan–Boltzmann constant $(W.m^{-2}.K^{-4})$

Γ Williamson relaxation time constant (s)

ξ Shear rate (s^{-1})

Π Second invariant of strain tensor (s^{-2})

δ Angle of inclination of the magnetic field (rad)

ω Angle of inclination of the sheet (rad)

λ_T Coefficient of thermal-relaxation time (s)

λ_C Coefficient of solutal-relaxation time (s)

λ_1 Thermal-relaxation parameter

λ_2 Solutal-relaxation parameter

Subscripts

w Condition at the wall surface

∞ Ambient or free-stream conditions far from the surface.

T Related to thermal effects

C Related to concentration (solutal) effects

r Radiative component

x Local variation along the x-direction

xx, xy Components of stress or strain tensors

Superscripts

$'$ Derivative with respect to the similarity variable η

$*$ Denotes a constant or mean value

Introduction

A fundamental component of contemporary fluid dynamics research, boundary layer flows of non-Newtonian fluids across a stretching surface have significant potential implications for a variety of engineering areas. Polymer extrusion, wire drawing, glass blowing, metal spinning and the aerodynamic extrusion of plastic sheets are just a few of industrial activities that frequently use these flows. The management of interfacial heat and mass transfer kinetics is closely related to the quality of the end products in such processing. By utilizing the interaction between an applied magnetic field and an electrically conducting fluid, magnetohydrodynamics (MHD) offers an effective flow control technique. This idea is utilized in MHD power generators, nuclear reactor cooling and materials processing. Simultaneously, the development of nanofluids, which are engineered colloidal suspensions of nanoparticles in a base fluid, has greatly increased the thermal conductivity of traditional coolants, offering up new possibilities in thermal management. The current manuscript investigates the complex interactions between heat and mass transfer by analyzing the unsteady MHD flow of a Williamson nanofluid over a permeable inclined stretching sheet and applying the advanced Cattaneo–Christov double-diffusion model for a more accurate representation of these phenomena.

The flow of pseudoplastic materials with shear-thinning properties, that is, materials whose apparent viscosity reduces with increasing shear rate, is commonly described by the Williamson fluid model. In theory, this model is

better than the power-law model since it avoids the singularity at zero shear rates by taking into account both minimum and maximum viscosities. This constitutive relation was first put forth by Williamson [1] in order to more accurately simulate the movement of pseudoplastic fluids in industrial pipelines. Over the years, the dynamics of Williamson fluid flow under different physical conditions have been widely studied. Shateyi and Muzara [2] used the Spectral Relaxation Method (SRM) to investigate the fundamental aspects of unsteady MHD boundary layer flow and heat transport over a stretching sheet. Using the shooting approach, Abbas et al. [3] expanded this field to nanofluids by examining the role of heat generation and viscous dissipation over a non-linear stretched sheet embedded in a porous medium. Muzara and Shateyi [4] used the Spectral Relaxation Method again to analyze flow over an exponentially stretching surface subject to thermal radiation and chemical reactions, while Geetha et al. [5] investigated double stratification effects across shrinking and stretching sheets using a shooting technique based on Runge-Kutta. Most recently, Kumar et al. [6] studied on Williamson fluid flow with Newtonian heating and heat source/sink interactions using the Runge-Kutta-Fehlberg (RKF-45) method. However, a thorough examination of the literature indicates that the cumulative interaction of unsteadiness and mixed convection for a Williamson nanofluid with geometry involving both an inclined sheet and an inclined magnetic field has not been simultaneously explored.

Choi [7] pioneered nanofluids, which involve dispersing metallic or oxide nanoparticles (such Cu, Al2O3, or TiO_2) in base fluids to achieve thermal conductivities up to 20–30% higher than conventional fluids. Theoretically, a popular model that combines thermophoresis and Brownian diffusion was presented by Buongiorno [8] to represent the microscopic processes that lead to enhanced mass and heat transport. Later study enhanced Williamson nanofluid flows by examining more comprehensive physical effects and employing various kinds of computational techniques. Ahmed and Akbar [9] and Buzuzi et al. [10] used the built-in MATLAB solver bvp4c, which implements a finite difference code based on the three-stage Lobatto IIIa formula, to solve their respective boundary layer models, concentrating on exponentially stretched and inclined sheets. Sankari et al. [11] investigated bioconvective fluxes in porous media using the spectral collocation method. More recently, Arif et al. [12] presented a stochastic computing paradigm that models cross-diffusion effects using Morlet wavelet neural networks optimized by particle swarm algorithms. The simultaneous characterization of unsteadiness and Cattaneo-Christov double-diffusion fluxes for a Williamson nanofluid is still a crucial research gap despite these thorough investigations. In particular, this unsteady rheological model over a doubly inclined geometry, which includes both magnetic field inclination and sheet inclination while collectively accounting for Joule heating, Soret and Dufour effects, thermal radiation and chemical reaction, has never been studied before. This is the main focus of the current work.

Magnetohydrodynamics (MHD), a fundamental concept in engineering applications such as nuclear reactor cooling and metallurgical processing, describes the complex interaction between electrically conducting fluids and magnetic

fields. Subsequent research has extended these frameworks by enhancing the mathematical and numerical knowledge of MHD Williamson fluid flows across stretching and shrinking surfaces. Magnetohydrodynamic (MHD) Williamson fluid flow over an exponentially stretching sheet was analyzed by Rao et al. [13] using the Runge-Kutta method in conjunction with a shooting scheme and the dynamics of unsteady MHD Casson and Williamson nanofluids were investigated by Divya et al. [14] using similar numerical integration techniques. Building on these approaches, Kumar et al. [15] used a shooting-based technique to study cross-diffusion phenomena in Williamson nanofluids in a permeable medium, while Sujatha and Sridhar [16] used numerical solvers to deal with dual stratification and Joule heating. Despite these substantial contributions, a careful analysis shows that there is still much to be explored about the simultaneous interplay of non-Fourier transport mechanisms and geometric inclination. In particular, the combined effects of an inclined stretched sheet and an inclined magnetic field under the Cattaneo-Christov heat and mass flux models have not yet been investigated in the literature. By including these characteristics into an unsteady framework that notably incorporates Soret, Dufour and Joule heating effects, the current study seeks to fill this gap.

The concept of permeability, a measurement of its capacity to permit fluid movement through interconnected pore networks, was first presented by Darcy [17] in his innovative work on fluid transport through porous structures. Subsequent research enhanced these models by integrating non-Newtonian rheology and advanced computational methods. For instance, Alrihieli et al. [18] used the shooting technique to examine MHD dissipative Williamson nanofluid flow with chemical reaction on a slippery elastic sheet. Khader et al. [19] advanced this field by employing the spectral collocation method to model Williamson nanofluid flow across an exponentially stretched sheet subject to slip velocity. Furthermore, Prithvi et al. [20] employed the Chebyshev Wavelet operational matrix method to examine the heat and mass transfer of MHD Williamson fluid over a porous stretching sheet, while Aroloye [21] examined thermal radiation and heat generation effects in hydro-magnetized Williamson fluid using the Runge-Kutta fourth-order method in conjunction with the shooting technique. A critical review of the literature reveals that the unsteady flow of a Williamson nanofluid integrating Cattaneo-Christov heat and mass flux relaxations over an inclined stretching sheet has not yet been studied. Specifically, the combined effects of mixed convection, Soret and Dufour effects, Joule heating and the magnetic field's inclination angle are not addressed by this specific constitutive framework.

The non-Fourier-non-Fick Cattaneo-Christov heat and mass flow models [22, 23], which add thermal and solutal relaxation times for hyperbolic transport analysis, are the outcome of a prevalent modification of the classical Fourier's and Fick’s rules of heat conduction to resolve the problem of infinite propagation speed. These models were improved in later studies to examine intricate rheological processes, especially in non-Newtonian Williamson fluids. Khan et al. [24] used the built-in-shooting method to examine slip flow regimes in a porous media in their

investigation of these flows. Abbas et al. [25] used the shooting approach with a Runge-Kutta-Fehlberg (RKF45) integration strategy, moving toward numerical schemes to solve extremely non-linear dissipative systems. Salahuddin et al. [26] and Salahuddin and Awais [27] improved this numerical method by effectively simulating double stratification and Joule heating effects using the MATLAB built-in bvp4c collocation algorithm. In order to assess the thermal performance of radiative MHD flows incorporating motile microorganisms, Malleswari et al. [28] most recently expanded these computer studies utilizing Runge-Kutta based numerical approaches. Despite these significant computational efforts, a critical review of the literature indicates that the unsteady transport of Williamson fluid that concurrently accounts for the geometric complexity of an inclined magnetic field and an inclined sheet while fully accounting for the coupled effects of Soret and Dufour cross-diffusion, Joule heating and chemical reaction under the influence of suction/injection has not yet been studied.

There is a noticeable research gap in the literature review mentioned above. Aspects of MHD, nanofluids, non-Newtonian models, porous media and Cattaneo–Christov theories have all been studied separately, but there isn't a single analysis that takes these factors into account. In particular, while taking into account thermal radiation, Joule heating, heat source, chemical reaction, Dufour and Soret effects, the unsteady MHD flow of a Williamson nanofluid over a permeable inclined stretching sheet under the influence of the Cattaneo–Christov double-diffusion model is still unexplored. This manuscript aims to bridge this gap by developing a robust mathematical model to investigate the effects of the critical parameters: Weissenberg number, unsteadiness, magnetic parameter, porosity, Grashof numbers, Prandtl, radiation, Brownian, thermophoresis, Eckert, Joule heating, Dufour, heat source, Schmidt, reaction, Soret, suction/injection, magnetic inclination, sheet inclination and relaxation times on the velocity, temperature and concentration fields as well as the skin friction, Nusselt number and Sherwood number. It is anticipated that the findings will have a major impact on the development of advanced materials processing systems, high-performance cooling devices and efficient chemical separation techniques.

Mathematical Formulations

In this work, the unsteady boundary layer flow of an incompressible Williamson nanofluid in 2D is examined. A permeable, linearly stretching sheet imbedded in a porous media generates the flow. The coordinate system is designed so that the y-axis is perpendicular to the surface and the x-axis is aligned with the direction of the sheet's stretching motion. ω represents the acute angle at which the sheet is inclined with respect to the horizontal plane. The stretching motion of the sheet is represented by the velocity u_w. The physical model illustrates how this velocity, which is time-dependent, can be described as (see Figure 1): $u_w = \frac{ax}{1-dt}$, where a and d represent positive constants, with d having the dimension of inverse time. The physical validity of the unsteady motion is ensured by imposing the requirement $dt < 1$.

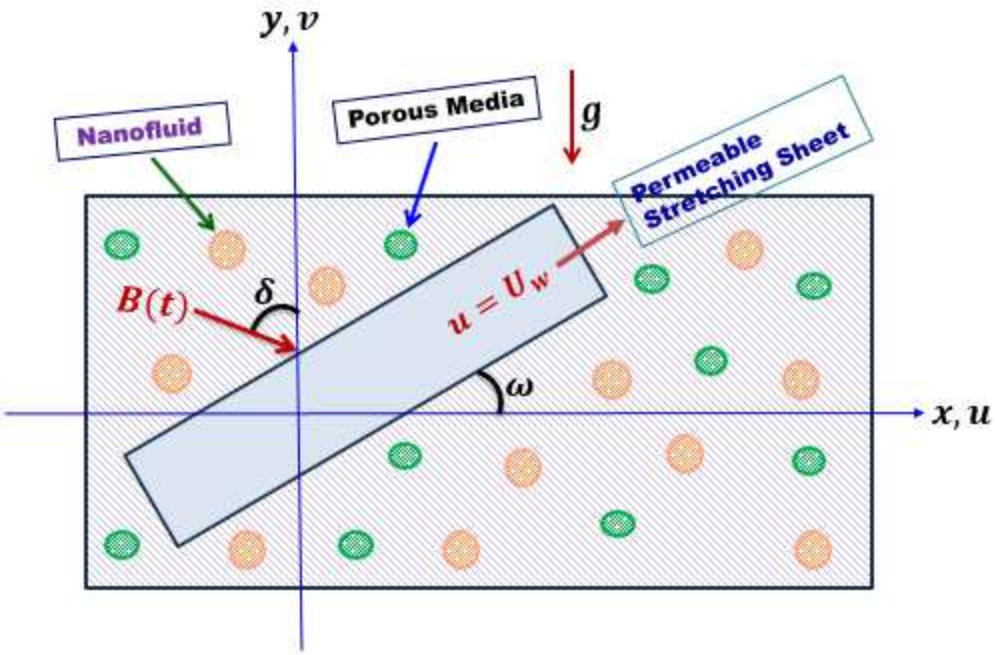


Fig. 1: Flow geometry and coordinate system

The fluid velocity, temperature, and nanoparticle concentration are maintained at U_w, T_w and C_w, respectively, at the wall. When the temperature and concentration are far from the sheet, the ambient values become T_∞ and C_∞, respectively. The system is subjected to an external magnetic field that changes over time and is determined by: $B(t) = \frac{B_0}{\sqrt{1-dt}}$, where B_0 stands for the magnetic field's initial strength. This field is applied with respect to the transverse axis (y-axis) with an inclination angle δ. The induced magnetic field is seen to be negligible in relation to the externally applied field, which is consistent with the low magnetic Reynolds number value.

We use the Williamson flow model to simulate the rheological behavior of the non-Newtonian fluid. According to [29], the Cauchy stress tensor, S, is defined as

$$\boldsymbol{S} = -P\boldsymbol{I} + \tau, \tag{1}$$

where P stands for isotropic pressure, $\boldsymbol{I}$ for identity tensor and τ for the extra stress tensor. The extra stress tensor for a Williamson fluid is expressed as follows:

$$\tau = \left(\mu_\infty + \frac{\mu_0 - \mu_\infty}{1 - \Gamma\xi}\right)\mathbb{A}_1, \tag{2}$$

where μ_0 denotes the zero-shear rate viscosity limit, μ_∞ represents the infinite shear rate viscosity limit, Γ (where $\Gamma > 0$) is the relaxation time constant, ξ corresponds to the shear rate and $\mathbb{A}_1$ designates the first Rivlin-Ericksen tensor.

The mathematical definition of the shear rate ξ is:

$$\xi = \sqrt{\sum_i \sum_j \xi_{ij}\,\xi_{ji}} = \sqrt{\frac{\Pi}{2}}, \tag{3}$$

where

$$\Pi = Trace\left(\mathbb{A}_1{}^2\right) \tag{4}$$

is referred to as the second invariant of the strain tensor.

In order to simplify the governing equations, we assume that the infinite shear rate viscosity $\mu_\infty = 0$ and that the product of the shear rate and time constant is modest ($\Gamma\xi < 1$). A binomial series expansion is used to reduce Equation (2) to:

$$\tau = \mu_0(1 + \Gamma\xi)\mathbb{A}_1. \tag{5}$$

This simplified model yields the non-zero elements of the extra stress tensor in the following manner:

$$\left.\begin{aligned} \tau_{xx} = 2\mu_0(1+\Gamma\xi)\frac{\partial u}{\partial x}, \tau_{yy} = 2\mu_0(1+\Gamma\xi)\frac{\partial v}{\partial y} \\ \tau_{xy} = \tau_{yx} = \mu_0(1+\Gamma\xi)\left(\frac{\partial u}{\partial y} + \frac{\partial v}{\partial x}\right) \end{aligned}\right\} \tag{6}$$

and $\tau_{xz} = \tau_{zx} = \tau_{yz} = \tau_{zy} = \tau_{zz} = 0$.

The following governing equations for continuity, momentum, energy and mass are established using the previously specified assumptions [29, 30]:

$$\frac{\partial u}{\partial x} + \frac{\partial v}{\partial y} = 0 \tag{7}$$

$$\frac{\partial u}{\partial t} + u\frac{\partial u}{\partial x} + v\frac{\partial u}{\partial y} = \upsilon\frac{\partial^2 u}{\partial y^2} + \sqrt{2}\upsilon\Gamma\frac{\partial u}{\partial y}\frac{\partial^2 u}{\partial y^2} - \left[\frac{\boldsymbol{\sigma}{B_0}^2 sin^2(\delta)}{\rho(1-dt)} + \frac{\upsilon}{K_0}\right]u + g\beta_T(T-T_\infty)cos(\omega) + g\beta_C(C-C_\infty)cos(\omega) \tag{8}$$

$$\frac{\partial T}{\partial t} + u\frac{\partial T}{\partial x} + v\frac{\partial T}{\partial y} = \alpha_f\frac{\partial^2 T}{\partial y^2} + \tau\left[D_B\frac{\partial C}{\partial y}\frac{\partial T}{\partial y} + \frac{D_T}{T_\infty}\left(\frac{\partial T}{\partial y}\right)^2\right] - \left(\frac{1}{\left(\rho c_p\right)_f}\frac{\partial q_r}{\partial y}\right) + \frac{\mu}{\left(\rho c_p\right)_f}\left(\frac{\partial u}{\partial y}\right)^2 + \frac{\boldsymbol{\sigma}{B_0}^2u^2}{\rho c_p} + \frac{D_m\mathbb{k}_T}{Csc_p}\frac{\partial^2 C}{\partial y^2} + \frac{Q_0(T-T_\infty)}{\left(\rho c_p\right)_f} - \lambda_T\left[\frac{\partial}{\partial t}\left(\frac{\partial T}{\partial t} + u\frac{\partial T}{\partial x} + v\frac{\partial T}{\partial y}\right) + u\frac{\partial}{\partial x}\left(\frac{\partial T}{\partial t} + u\frac{\partial T}{\partial x} + v\frac{\partial T}{\partial y}\right) + v\frac{\partial}{\partial y}\left(\frac{\partial T}{\partial t} + u\frac{\partial T}{\partial x} + v\frac{\partial T}{\partial y}\right)\right] \tag{9}$$

$$\frac{\partial C}{\partial t} + u\frac{\partial C}{\partial x} + v\frac{\partial C}{\partial y} = D_B\frac{\partial^2 C}{\partial y^2} + \frac{D_T}{T_\infty}\frac{\partial^2 T}{\partial y^2} + \frac{D_m\mathbb{k}_T}{T_m}\frac{\partial^2 T}{\partial y^2} - Kr(C-C_\infty) - \lambda_C\left[\frac{\partial}{\partial t}\left(\frac{\partial C}{\partial t} + u\frac{\partial C}{\partial x} + v\frac{\partial C}{\partial y}\right) +\right.$$

$$u\frac{\partial}{\partial x}\left(\frac{\partial C}{\partial t}+u\frac{\partial C}{\partial x}+v\frac{\partial C}{\partial y}\right)+v\frac{\partial}{\partial y}\left(\frac{\partial C}{\partial t}+u\frac{\partial C}{\partial x}+v\frac{\partial C}{\partial y}\right)\Bigg] \tag{10}$$

The following describes the related boundary conditions that apply to this situation [29].

At $y=0$,

$$u=U_w(x,t)=\frac{ax}{1-dt}, v=V_w(x,t)=-\frac{V_0}{\sqrt{1-dt}}, T=T_w(x,t)=T_\infty+\frac{T_0V_wx}{v\sqrt{1-dt}},$$

$$C=C_w(x,t)=C_\infty+\frac{C_0V_wx}{v\sqrt{1-dt}} \tag{11}$$

and as $y\to\infty$,

$$u\to 0, \qquad T\to T_\infty, \qquad C\to C_\infty \tag{12}$$

where t denotes the time variable, v represents kinematics viscosity, μ represents dynamic viscosity, g is the gravitational acceleration, β_T and β_C are the coefficients of thermal and solutal volumetric expansion, respectively; K_0 signifies the permeability of the porous medium, α_f denotes the thermal diffusivity of the fluid, T and C coresspond to the fluid temperature and concentration of the fluid, respectively; ρ is the fluid density, c_p is the specific heat capacity at constant pressure and $(\rho c_p)_f$ refers to the volumetric heat capacity of the fluid. Furthermore, the symbols q_r, $\boldsymbol{\sigma}$, D_m, Cs, D_T, Q_0, $\mathbb{k}_T$, T_m, Kr, λ_T and λ_C represent, respectively, radiative heat flux, the electrical conductivity of the fluid, the molecular diffusivity of species concentration, the concentration susceptibility, the thermophoretic diffusion coefficient, the heat source coefficient, the thermal diffusion ratio, the mean temperature, the chemical reaction rate, coefficient of thermal-relaxation time and coefficient of solutal-relaxation time. The dimensionless parameter τ represents the ratio of the volumetric heat capacity of the nanoparticles to that of the base fluid, defined as $\tau=\frac{(\rho c_p)_p}{(\rho c_p)_f}$, where $(\rho c_p)_p$ and $(\rho c_p)_f$ represent the volumetric heat capacities of the nanoparticle and the base fluid, respectively.

The mathematical expression for radiative heat flux can be simplified by using the Rosseland approximation as [29].

$$q_r=-\frac{4\sigma^*}{3\hbar^*}\frac{\partial T^4}{\partial y} \tag{13}$$

where, the symbols σ^* and $\hbar^*$ denote the Stefan–Boltzmann constant and the mean thermal absorption coefficient, respectively.

The following approximation is obtained by using a Taylor series expansion about the free stream temperature and ignoring higher order terms, assuming that the temperature variation within the boundary layer is small enough to disregard higher-order terms.

$$T^4 \cong 4{T_\infty}^3 T - 3{T_\infty}^4 \tag{14}$$

According to Equations (13) and (14),

$$\frac{\partial q_r}{\partial y} \cong -\frac{16\sigma^* {T_\infty}^3}{3\hbar^*}\frac{\partial^2 T}{\partial y^2} \tag{15}$$

Using Eq. (15), the energy equation (Eq. (9)) is rewritten as follows.

$$\frac{\partial T}{\partial t} + u\frac{\partial T}{\partial x} + v\frac{\partial T}{\partial y} = \alpha_f \frac{\partial^2 T}{\partial y^2} + \tau\left[D_B \frac{\partial C}{\partial y}\frac{\partial T}{\partial y} + \frac{D_T}{T_\infty}\left(\frac{\partial T}{\partial y}\right)^2\right] + \left(\frac{16\sigma^* {T_\infty}^3}{3\hbar^*\left(\rho c_p\right)_f}\frac{\partial^2 T}{\partial y^2}\right) + \frac{\mu}{\left(\rho c_p\right)_f}\left(\frac{\partial u}{\partial y}\right)^2 +$$

$$\frac{\boldsymbol{\sigma}{B_0}^2 u^2}{\rho c_p} + \frac{D_m \mathbb{k}_T}{C s c_p}\frac{\partial^2 C}{\partial y^2} + \frac{Q_0(T - T_\infty)}{\left(\rho c_p\right)_f} - \lambda_T\left[\frac{\partial}{\partial t}\left(\frac{\partial T}{\partial t} + u\frac{\partial T}{\partial x} + v\frac{\partial T}{\partial y}\right) + u\frac{\partial}{\partial x}\left(\frac{\partial T}{\partial t} + u\frac{\partial T}{\partial x} + v\frac{\partial T}{\partial y}\right) + v\frac{\partial}{\partial y}\left(\frac{\partial T}{\partial t} + u\frac{\partial T}{\partial x} + v\frac{\partial T}{\partial y}\right)\right] \tag{16}$$

By using the following suitable similarity transformations, the governing equations can be reduced to a system of ordinary differential equations.

$$\eta = y\sqrt{\frac{U_w}{\upsilon x}},\ \psi(x,y,t) = \sqrt{U_w \upsilon x} f(\eta), \theta(\eta) = \frac{T - T_\infty}{T_w - T_\infty}, \phi(\eta) = \frac{C - C_\infty}{C_w - C_\infty}, \tag{17}$$

where, η denotes the dimensionless similarity variable, $f(\eta)$ represents the dimensionless stream function, while $\theta(\eta)$ and $\phi(\eta)$ correspond to the dimensionless temperature and nanoparticle volumetric fraction, respectively. The stream function, represented by ψ, has been assigned so that $u = \frac{\partial \psi}{\partial y}$ and $v = -\frac{\partial \psi}{\partial x}$ are the velocity components in the x- and y-directions, respectively. Thus,

$$u = U_w f'(\eta), \qquad v = -\sqrt{\frac{U_w \upsilon}{x}} f(\eta). \tag{18}$$

Eq. (7) is automatically verified by using the transformations described in Eqs. (17-18) and Eqs. (8, 10, 16) and the boundary conditions given in Eq. (11) take on the following forms.

$$(1 + We f'')f''' + \left(f - \frac{A\eta}{2}\right)f'' - (f')^2 - (A + M^2 sin^2(\delta) + Kp)f' + (Gr_T\theta + Gr_C\phi)cos(\omega) = 0 \tag{19}$$

$$\frac{1}{Pr}\left(1 + \frac{4}{3}Rd\right)\theta'' + f\theta' - f'\theta - A\left(\theta + \frac{\eta}{2}\theta'\right) + Nb\theta'\phi' + Nt(\theta')^2 + Du\phi'' + Ec(f'')^2 + JH(f')^2 +$$

$$\mathbb{Q}\theta - \lambda_1\left[\left(f - \frac{1}{2}A\eta\right)^2\theta'' + \left(\frac{1}{2}A\eta f' - ff' - \frac{7}{2}Af + \frac{7}{4}A^2\eta\right)\theta' + \left((f')^2 + 3Af' + \left(\frac{A\eta}{2} - f\right)f'' + 2A^2\right)\theta\right] = 0 \tag{20}$$

$$\frac{1}{Sc}\phi'' + \left(f - \frac{A\eta}{2}\right)\phi' - (f' + A + \gamma)\phi + (Nt + Sr)\theta'' - \lambda_2\left[\left(f - \frac{1}{2}A\eta\right)^2\phi'' + \left(\frac{1}{2}A\eta f' - ff' - \frac{7}{2}Af +\right.\right.$$

$$\frac{7}{4}A^2\eta\Big)\phi' + \Big((f')^2 + 3Af' + \Big(\frac{A\eta}{2} - f\Big)f'' + 2A^2\Big)\phi\Big] = 0 \tag{21}$$

where f, θ and ϕ are functions of η, with primes denoting derivatives with respect to η. The boundary conditions associated with these functions will be expressed in the following form:

$$\left.\begin{array}{c} f(0) = S, f'(0) = 1, \theta(0) = 1, \phi(0) = 1 \\ f'(\infty) = 0, \theta(\infty) = 0, \phi(\infty) = 0 \end{array}\right\} \tag{22}$$

where $We = \Gamma\sqrt{\frac{U_w^3}{\upsilon x}}$ is the Weissenberg number representing the Williamson number, $A = \frac{d}{a}$ is the unsteadiness parameter, $M^2 = \frac{\boldsymbol{\sigma}{B_0}^2 x}{\rho_f U_w}$ is the magnetic parameter, $Kp = \frac{\upsilon x}{U_w K_0}$ is the porosity parameter, $Gr_T = \frac{g\beta_T(T_w - T_\infty)x}{U_w^2}$ is the thermal Grashof number, $Gr_C = \frac{g\beta_C(C_w - C_\infty)x}{U_w^2}$ is the mass Grashof number, $Pr = \frac{\upsilon}{\alpha_f}$ is the Prandtl number, $Rd = \frac{4\sigma^* {T_\infty}^3}{k\hbar^*}$ is the thermal radiation parameter, $Nb = \frac{\tau D_B(C_w - C_\infty)}{\upsilon}$ is the Brownian parameter, $Nt = \frac{\tau D_T(T_w - T_\infty)}{\upsilon T_\infty}$ is the thermophoresis parameter, $Ec = \frac{{U_w}^2}{(c_p)_f(T_w - T_\infty)}$ is Eckert number, $JH = \frac{\boldsymbol{\sigma}{B_0}^2 U_w x}{\rho c_p(T_w - T_\infty)}$ is the Joule heating parameter, $Du = \frac{D_m \mathbb{k}_T(C_w - C_\infty)}{\upsilon C s c_p(T_w - T_\infty)}$ is the Dufour number, $\mathbb{Q} = \frac{Q_0 x}{\rho c_p U_w}$ is the heat source parameter, $Sc = \frac{\upsilon}{D_B}$ is the Schmidt number, $\gamma = \frac{Krx}{U_w}$ is the chemical reaction parameter (with $\gamma > 0$ and $\gamma < 0$ denoting destructive and generating chemical reaction rates, respectively), $Sr = \frac{D_m \mathbb{k}_T(T_w - T_\infty)}{\upsilon T_m(C_w - C_\infty)}$ is the Soret number, $S = \frac{V_0}{\sqrt{a\upsilon}}$ is the suction/injection parameter ($S > 0$ suction and $S < 0$ injection), $\lambda_1 = \frac{a(\lambda_T)}{1-dt}$ is thermal-relaxation parameter and $\lambda_2 = \frac{a(\lambda_C)}{1-dt}$ is solutal-relaxation parameter.

For empirical investigations, the dimensionless parametrs, namely the skin friction coefficient Cf, the Nusselt number Nu_x and the Sherwood number Sh_x are introduced. These quantities are defined and interpreted as follows

$$Cf = \frac{\tau_w}{(1/2)\rho_f {U_w}^2}, \qquad Nu_x = \frac{xq_w}{k(T_w - T_\infty)}, \qquad Sh_x = \frac{xq_m}{D_B(C_w - C_\infty)} \tag{23}$$

where, the terms τ_w (wall shear stress), q_w (surface heat flux) and q_m (wall mass flux) are expressed as:

$$\tau_w = -\mu_0\left[\frac{\partial u}{\partial y} + \frac{\Gamma}{\sqrt{2}}\Big(\frac{\partial u}{\partial y}\Big)^2\right]_{y=0}, \qquad q_w = -\left(k + \frac{16{T_\infty}^3\sigma^*}{3\hbar^*}\right)\left[\frac{\partial T}{\partial y}\right]_{y=0}, \qquad q_m = D_B\left[\frac{\partial T}{\partial y}\right]_{y=0} \tag{24}$$

By employing the dimensionless variables defined in Eqs. (17-18), we obtain

$$\left.\begin{array}{c} \sqrt{Re_x}Cf = -f''(0)\big(2 + Wef''(0)\big) \\ Nu_x = -\sqrt{Re_x}\left(1 + \frac{4}{3}Rd\right)\theta'(0) \\ Sh_x = -\sqrt{Re_x}\phi'(0) \end{array}\right\} \tag{25}$$

where $Re_x = \frac{ax^2}{\upsilon(1-dt)}$ represents the local Reynold number.

Solution Methodology

We use the optimal homotopy analysis method (OHAM) to establish semi-analytical approximations for the nonlinear systems given in Eqs. (19–21) with the relevant boundary conditions, Eq. (22). OHAM is a rigorous evolution of the pioneering homotopy analysis method (HAM) proposed by Liao [31, 32], which was crucial for reducing the dependence on small physical parameters required by standard perturbation methods. OHAM offers a more objective framework for choosing a convergence control parameter, whereas regular homotopy analysis method (HAM) frequently depends on a subjective, trial and error method. The technique creates a versatile auxiliary function with several convergence constants that are defined mathematically rather than chosen at random. This invention replaces the human examination of convergence curves in the solution process with a dependable and methodical optimization approach. OHAM uses the method of least squares to minimize the residual error in order to determine the ideal values for its convergence constants rather than guessing parameters. Since its inception, OHAM has been widely accepted and successfully applied to a wide range of nonlinear ODEs, PDEs, differential-difference equations and even issues that arise in finance and other fields [32–34]. It has become one of the best semi-analytical tools available for substantially nonlinear problems due to its flexibility, rigorous convergence theory and capacity to provide extremely precise analytical approximations.

The technique makes use of auxiliary linear operators, which are defined as

$$L_f = \frac{d^3f}{d\eta^3} + \frac{d^2f}{d\eta^2}, \qquad L_\theta = \frac{d^2\theta}{d\eta^2} + \frac{d\theta}{d\eta}, \qquad L_\phi = \frac{d^2\phi}{d\eta^2} + \frac{d\phi}{d\eta} \tag{26}$$

in accordance with the conditions set forth

$$L_f[C_1 + C_2\eta + C_3 exp(-\eta)] = 0 \tag{27}$$

$$L_\theta[C_4 + C_5 \exp(-\eta)] = 0 \tag{28}$$

$$L_\phi[C_6 + C_7 \mathrm{Exp}(-\eta)] = 0 \tag{29}$$

where, the specified boundary or initial conditions can be used to uniquely define the arbitrary constants represented by the coefficients C_i(where $i = 1, 2, \ldots, 7$).

Additionally, this technique requires a suitable initial guess, which is obtained using the boundary conditions described in Eq. (22) and the previously presented linear operators, which are considered to be

$$f_0 = S + 1 - \exp(-\eta), \qquad \theta_0 = \exp(-\eta), \qquad \phi_0 = \exp(-\eta). \tag{30}$$

The nonzero auxiliary functions can alternatively be expressed in the following way:

$$H_f(\eta) = H_\theta(\eta) = H_\phi(\eta) = \exp(-\eta). \tag{31}$$

The convergence control parameters $\hbar_f$, $\hbar_\theta$ and $\hbar_\phi$ must be carefully chosen in order for the OHAM solution to converge effectively. By reducing the discrete squared residual error, the ideal values of each parameter can be found within the given ranges as

$$\mathcal{E}_k(\hbar) \approx \frac{1}{1+N}\sum_{j=0}^{N}\left\{\aleph\left[\sum_{n=0}^{k} u_n(\eta_j)\right]\right\}^2. \tag{32}$$

Next, using the built-in functions of the BVPh 2.0 Mathematica package [34], the optimal values for the convergence control parameters of this particular problem are extracted.

$$\hbar_f \approx -0.573913, \qquad \hbar_\theta \approx -0.749601, \qquad \hbar_\phi \approx -0.545763 \tag{33}$$

As additional verification of convergence, Table 1 shows the squared residual errors for the selected situations.

Table 1: The numerical convergence of certain OHAM solutions when $We = Rd = Nb = Nt = Gr_T = Gr_C = \lambda_1 = \lambda_2 = 0.1, A = M = 0.3, Kp = Pr = 1.0, Sc = 0.6, \gamma = Ec = Du = 0.2, S = -0.1, Sr = JH = 0.5, \delta = \omega = \pi/6, Q = 0.4$

Order of Approximation	$-f''(0)$	$-\theta'(0)$	$-\phi'(0)$	ε_f	ε_θ	ε_ϕ
2	1.44222	0.965349	0.600090	2.8×10^{-5}	2.9×10^{-4}	4.6×10^{-4}
4	1.44115	0.929154	0.616087	5.2×10^{-8}	2.4×10^{-4}	1.8×10^{-4}
6	1.43979	0.902632	0.633631	6.6×10^{-7}	2.3×10^{-4}	8.3×10^{-5}
8	1.43937	0.883493	0.645202	6.2×10^{-7}	2.2×10^{-4}	3.5×10^{-5}
10	1.43907	0.869717	0.652444	3.0×10^{-7}	2.1×10^{-4}	1.4×10^{-5}
12	1.43883	0.859804	0.656730	2.1×10^{-7}	2.0×10^{-4}	6.2×10^{-6}
14	1.43863	0.852668	0.659024	1.5×10^{-7}	1.9×10^{-4}	4.7×10^{-6}
16	1.43846	0.847524	0.659997	1.3×10^{-7}	1.7×10^{-4}	4.2×10^{-6}
18	1.43832	0.843807	0.660111	1.1×10^{-7}	1.6×10^{-4}	3.9×10^{-6}
20	1.43820	0.841113	0.659683	1.0×10^{-7}	1.4×10^{-4}	3.6×10^{-6}
22	1.43809	0.839151	0.658932	1.0×10^{-8}	1.3×10^{-4}	3.4×10^{-6}

Order of Approximation	$-f''(0)$	$-\theta'(0)$	$-\phi'(0)$	ε_f	ε_θ	ε_ϕ
24	1.43799	0.837713	0.658001	9.8×10^{-8}	1.2×10^{-4}	3.2×10^{-6}
26	1.43791	0.836650	0.656985	9.6×10^{-8}	1.1×10^{-4}	3.1×10^{-6}
28	1.43783	0.835857	0.655956	9.3×10^{-8}	1.0×10^{-4}	2.9×10^{-6}
30	1.43776	0.835257	0.654993	9.1×10^{-8}	9.1×10^{-5}	2.8×10^{-6}

Table 1 makes it extremely evident that the terms of the series converge more closely, the squared residual errors decrease and convergence is reached at the 24th order of the OHAM approximation as the order of OHAM iteration increases.

More specifically, the overall error can also be calculated using the relationship

$$\varepsilon_k{}^t = \varepsilon_k{}^f + \varepsilon_k{}^\theta + \varepsilon_k{}^\phi \tag{34}$$

Figure 2 illustrates how the total inaccuracy decreases as the order of the OHAM approximation increases. As a result, the series solution keeps converging under successive higher order approximations in OHAM.

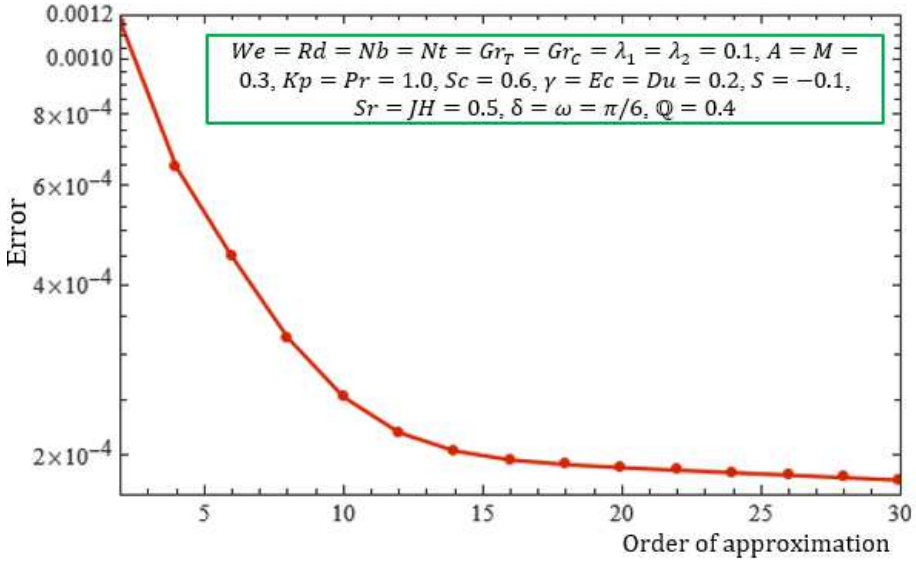


Fig. 2: Total squared residual error

The problem under consideration reduces to the situation studied by Shamshuddin et al. [35], Mukhopadhyay [36] and Mabood et al. [37] when the impact of other characteristics is excluded. As a result, we offer a comparison of the current study's results with those that have already been published.

The values of $-f''(0)$ acquired in the current study exhibit a remarkable agreement with those reported in the referred literature, according to the comparison analysis described in Table 2. This is usually seen as an essential element in ensuring the method's dependability.

Table 2: Comparison of the values of $-f''(0)$ for $A = We = Kp = Rd = \gamma = S = Ec = Nb = Nt = Du = Sr = Gr_T = Gr_C = JH = \mathbb{Q} = \lambda_1 = \lambda_2 = 0, \delta = \omega = \pi/2, Sc = Pr = 1.0$, against some values of M

M	Mukhopadhyay [36]	Mabood et al. [37]	Shamshuddin et al. [35]	Present study
0.5	1.1180	1.1180	1.118035	1.117881
1.0	1.4142	1.4142	1.414214	1.414195
1.5	1.8027	1.8027	1.802776	1.802778
2.0	2.2361	2.2361	2.236068	2.236068

Results and Discussion

This section explores the numerical and graphical outputs generated from the utilization of the OHAM of the dimensionless governing equations, namely Eqs. (19–21), under the given boundary conditions of Eq. (22). To effectively examine the impact of different flow parameters on the transport phenomena, a thorough parametric investigation has been carried out. The Weissenberg number, unsteadiness parameter, magnetic parameter, porosity parameter, thermal Grashof number, mass Grashof number, Prandtl number, thermal radiation parameter, Brownian parameter, thermophoresis parameter, Eckert number, Joule heating parameter, Dufour number, heat source parameter, Schmidt number, chemical reaction parameter, Soret number, suction/injection parameter, inclination angle of the magnetic field, inclination angle of the sheet, relaxation time of heat flux and relaxation time of mass flux are all extensively examined and their effects are graphically depicted in Figures 3- 22. In addition, Tables 3 methodically tabulate and examine resulting impacts of these essential components on the local skin friction coefficient $\left(\sqrt{Re_x}Cf\right)$, the local Nusselt number $\left(Nu_x/\sqrt{Re_x}\right)$, and the local Sherwood number $\left(Sh_x/\sqrt{Re_x}\right)$. The physical governing parameters implemented in this study fall into the following ranges: $0.0 \leq We \leq 1.4$, $0.0 \leq A \leq 2.0$, $-1.0 \leq S \leq 1.0$, $0.0 \leq Kp \leq 3.0$, $0.0 \leq M \leq 2.0$, $0.0 \leq \delta \leq 90$℃, $0.0 \leq \omega \leq 90$℃, $0.0 \leq Gr_T \leq 1.0$, $0.0 \leq Gr_C \leq 1.0, 0.0 \leq Pr \leq 3.0, 0.0 \leq Rd \leq 2.0, 0.0 \leq \mathbb{Q} \leq 2.0, 0.0 \leq Ec \leq 2.0, 0.0 \leq JH \leq 1.0, 0.0 \leq Sc \leq 2.0$, $0.0 \leq Nb \leq 3.0$, $0.0 \leq Nt \leq 3.0$, $-1.0 \leq \gamma \leq 2.0$, $0.0 \leq Du \leq 1.0$, $0.0 \leq Sr \leq 2.0$, $0.0 \leq \lambda_1 \leq 1.0$ and $0.0 \leq \lambda_2 \leq 1.0$. A baseline set of default values has been chosen for the controlling parameters: $We = Rd = Nb = Nt = Gr_T = Gr_C = \lambda_1 = \lambda_2 = 0.1$, $A = M = 0.3$, $Kp = Pr = 1.0$, $Sc = 0.62$, $\gamma = Ec = Du = 0.2$, $S = -0.1$, $Sr = JH = 0.5$, $\delta = \omega = \pi/6$ and $\mathbb{Q} = 0.4$ in order to make it easier to physically understand the findings in a clear and consistent manner. As a result, unless explicitly noted otherwise for a specific analysis, all tabular data and graphical representations in this document are based on these recommended values.

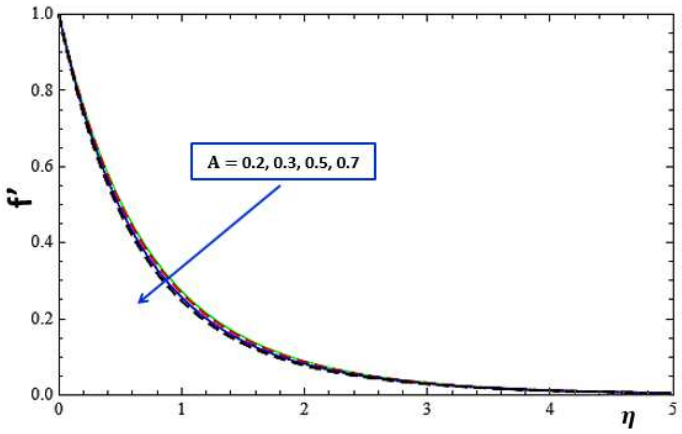


Fig. 3(a): Effect of unsteady parameter (A) on velocity profiles

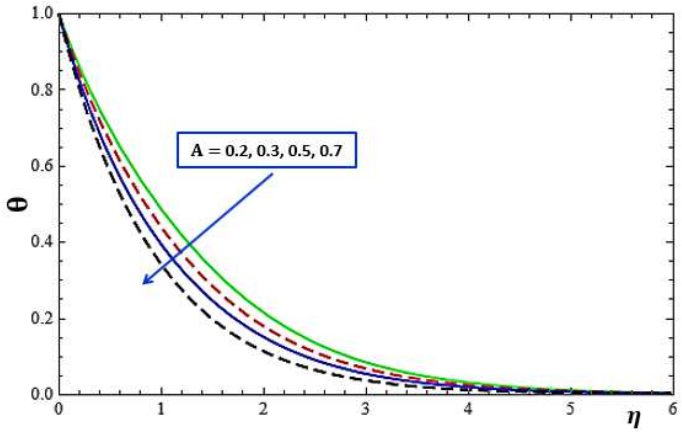


Fig. 3(b): Effect of unsteady parameter (A) on temperature profiles

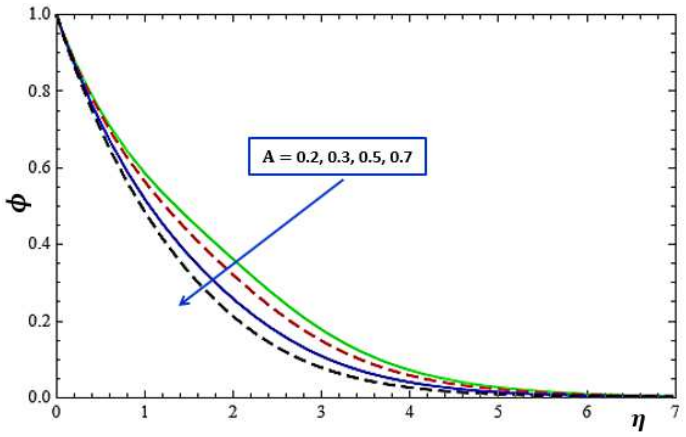


Fig. 3(c): Effect of unsteady parameter (A) on concentration profiles

Figures 3(a)-3(c) show how the unsteady parameter affects the velocity, temperature and concentration profiles. The unsteady parameter, which represents the ratio of transient effects to steady-state conditions and describes the flow's time-dependent nature, has a major influence on the fluid system's transport phenomena. As seen in Fig. 3(a),

the velocity profiles throughout the domain diminish slightly as A increases. This is explained by increased temporal resistance, in which sudden instability creates extra drag-like effects that prevent the fluid from moving forward. As seen in Fig. 3(b), the temperature profiles substantially drop as the unsteadiness parameter rises. This happens because the sheet dissipates more heat as the unsteadiness grows, lowering the fluid's temperature. In a similar way, concentration profiles fall noticeably as the unsteadiness parameter elevates. Lower species concentrations inside the boundary layer are the result of improved mass transport from the surface caused by the enhanced unsteadiness.

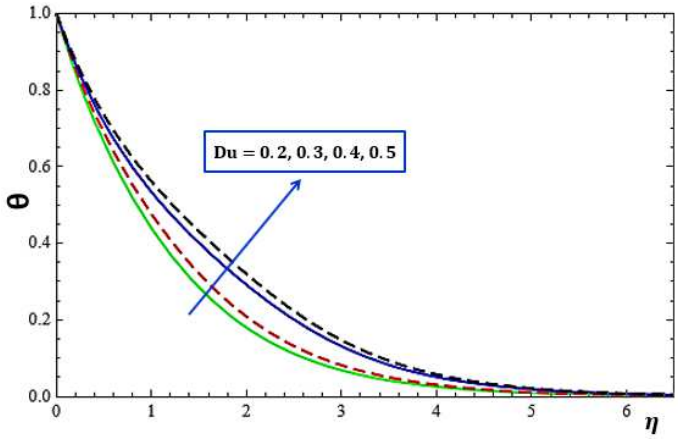


Fig. 4: Effect of Dufour number (Du) on temperature profiles

Figure 4 illustrates how the system's dimensionless temperature profiles are affected by the Dufour number. The diffusion-thermo effect, or Dufour number, quantifies to what extent the thermal energy flux is impacted by concentration gradients. There is a visible improvement in the temperature profiles throughout the domain as the Dufour number rises. This pattern results from the stronger correlation between thermal gradients and concentration, which intensifies the Dufour effect-driven heat transfer. As a result, the temperature rises and the thermal boundary layer thickens, emphasizing the importance of the diffusion-thermo effect in systems where mass and heat transfer occur simultaneously.

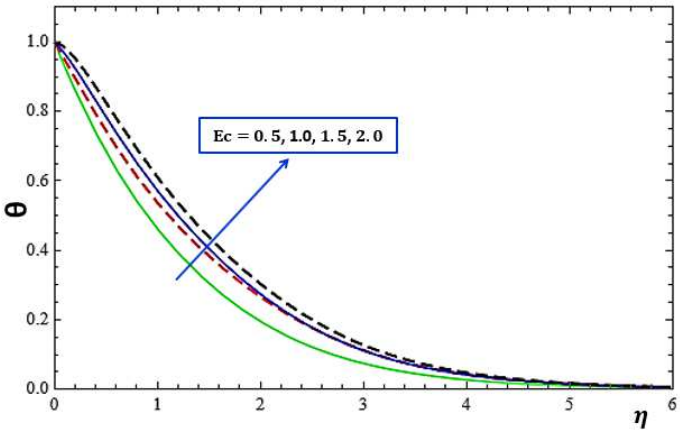


Fig. 5: Effect of Eckert number (Ec) on temperature profiles

Figure 5 depicts the effect of the Eckert number on the temperature profiles within the boundary layer. An essential tool for describing the thermal dissipation throughout the boundary layer, the Eckert number measures the ratio of kinetic energy to enthalpy. It is evident from the figure that temperature profiles throughout the domain enhanced when the Eckert number rises from 0.5 to 2.0. This is because fluid friction causes more energy to be dissipated when the Eckert number is elevated. The dissipated energy acts as an internal heat source, thereby the temperature profiles manifest an ongoing rise across the entire region. This result highlights the crucial significance of the Eckert number in regulating the behavior of the thermal boundary layer and its consequences for the system's heat transfer properties.

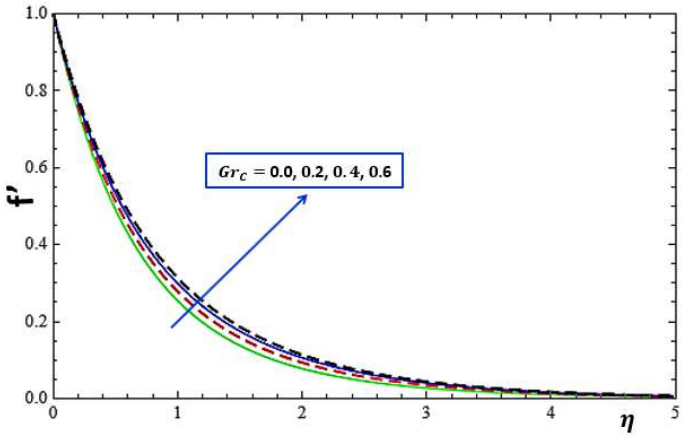


Fig. 6: Effect of solutal Grashof number (Gr_C) on velocity profiles

The impact of the solutal Grashof number on the fluid domain velocity profiles is seen in Figure 6. The solutal Grashof number, responsible for regulating the natural convection resulted due to species concentration variations, represents the ratio of buoyant forces resulting from concentration differences to viscous forces. The velocity profiles are shown to rise noticeably across the domain when the solutal Grashof number rises from 0.2 to 0.8. Such a rise in velocity is attributed to the fact that a higher solutal Grashof number signifies stronger buoyancy forces coming from concentration gradients, leading to accelerate fluid motion.

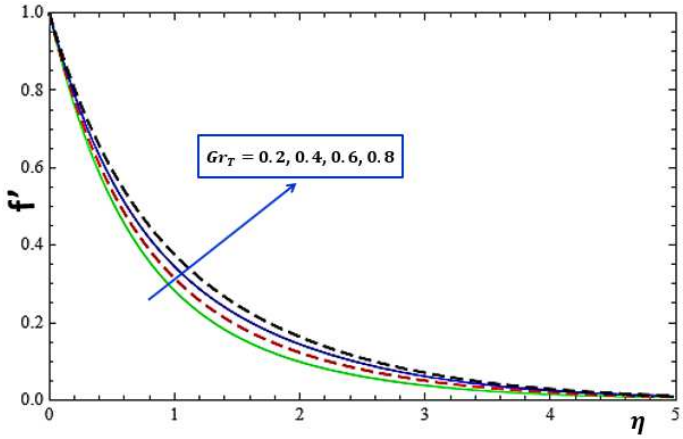


Fig. 7: Effect of thermal Grashof number (Gr_T) on velocity profiles

The effect of thermal Grashof number on velocity profiles is presented in Figure 7. Natural convection dynamics caused by temperature gradients is governed by the thermal Grashof number, which measures the proportion of buoyant forces to viscous forces in fluid systems. The plotted results make it evident that the velocity profiles rise steadily throughout the domain as the Grashof number increases. The observed trend results from increased buoyant forces surpassing viscous resistance, which facilitates fluid flow and intensifies convective currents.

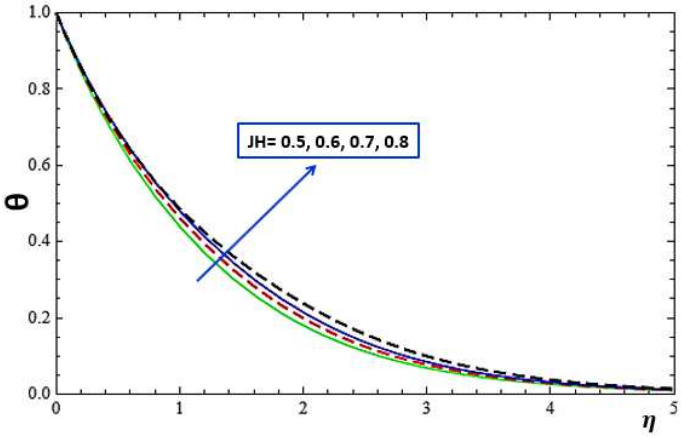


Fig. 8: Effect of Joule heating parameter (JH) on temperature profiles

The effect of the Joule heating parameter on the fluid system's temperature profiles is seen in Figure 8. The Joule heating parameter, which is directly related to the interaction between the electric current and the fluid's conductive characteristics, measures the thermal energy produced by electrical resistance within the fluid. A higher Joule heating parameter causes more heat to be generated, which raises the temperature profiles throughout the domain. The increased ohmic dissipation, which intensifies thermal energy production as JH rises, is responsible for this trend. As a result, the temperature profiles show a steady upward movement, signifying a thicker thermal boundary

layer. This trend highlights the crucial part that Joule heating plays in regulating the system's thermal properties and considerably affecting heat transmission mechanisms.

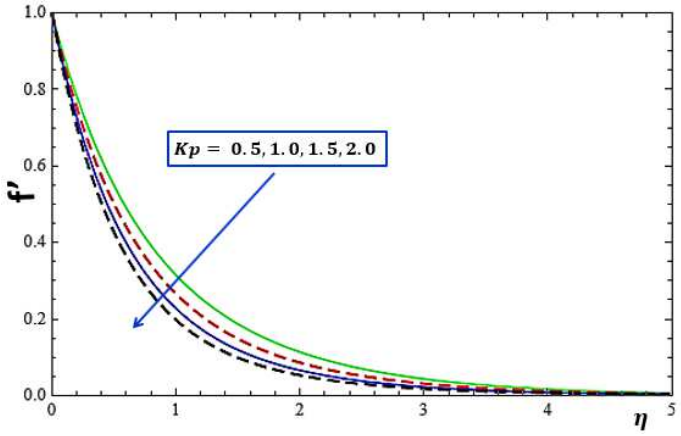


Fig. 9: Effect of porosity parameter (Kp) on velocity profiles

Figure 9 shows how the velocity profiles are affected by the porosity parameter. In the study of fluid flow through porous media, the porosity parameter—which indicates the resistance provided by the porous structure—is an essential non-dimensional quantity. According to Darcy's Law, this resistance is essentially related to the medium's permeability. The analyses conducted show explicitly that the fluid's velocity over the boundary layer reduces as the porosity parameter boosts. This tendency is physically acceptable since a larger porosity characteristic indicates more resistance from the porous material, i.e., The fluid motion is opposed by this increased resistance, which causes a drag-like effect known as the Darcy drag force, which causes the flow to slow down.

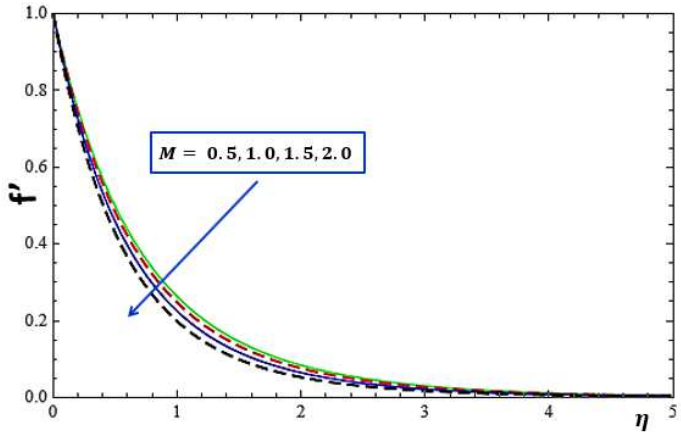


Fig. 10: Effect of magnetic field parameter (M) on velocity profiles

Figure 10 illustrates how the magnetic field parameter affects the velocity profiles. The strength of the applied magnetic field and its interaction with the electrically conducting nanofluid are measured by the magnetic field parameter, which is commonly denoted by M. As M rises, the velocity profiles across the flow region show a

significant decrease. This phenomenon is explained by the Lorentz force that the magnetic field produces, which resistively drags the fluid motion. As a result, the fluid's deceleration causes the momentum boundary layer's thickness to get thinner, which is crucial for regulating the system's transport phenomena.

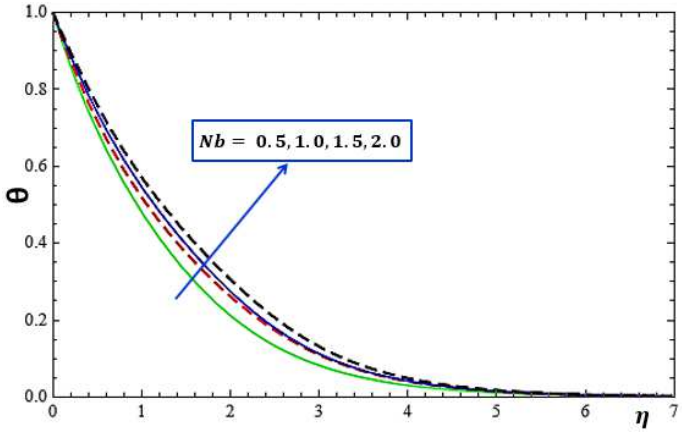


Fig. 11(a): Effect of Brownian motion parameter (Nb) on temperature profiles

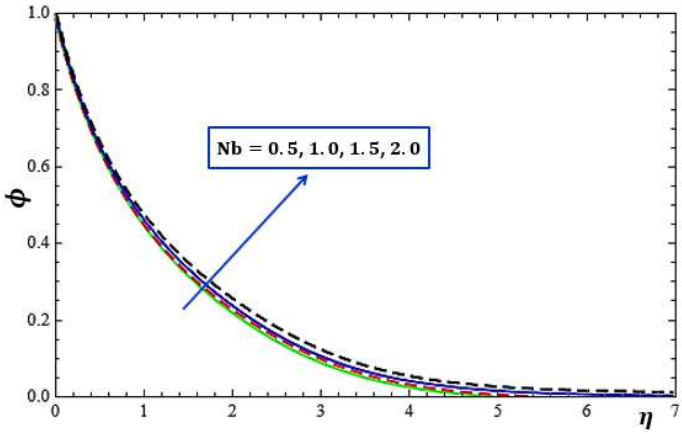


Fig. 11(b): Effect of Brownian motion parameter (Nb) on concentration profiles

Figures 11(a) and 11(b) show how the Brownian motion parameter affects the nanofluid's temperature and concentration profiles, respectively. The random microscopic movement of nanoparticles suspended in the base fluid is reflected by Brownian motion and the intensity of this motion has a direct impact on the mass and thermal transport characteristics of nanofluids. As seen in Figure 11(a), increasing the Brownian motion parameter promotes meaningfully the temperature profiles across the domain. The primary cause of this is the increased kinetic activity of the nanoparticles, which increases the fluid's capacity to carry energy and raises the local temperature distribution. In similar manner, the concentration profiles in Figure 11(b) show a modest rise when the Brownian motion parameter increases. The reason for this pattern is because the improved solute mobility brought about by the increased nanoparticle agitation increases particle concentration close to the boundary. These results

demonstrate the complex ways in which Brownian motion modulates heat and mass transport processes in nanofluid systems.

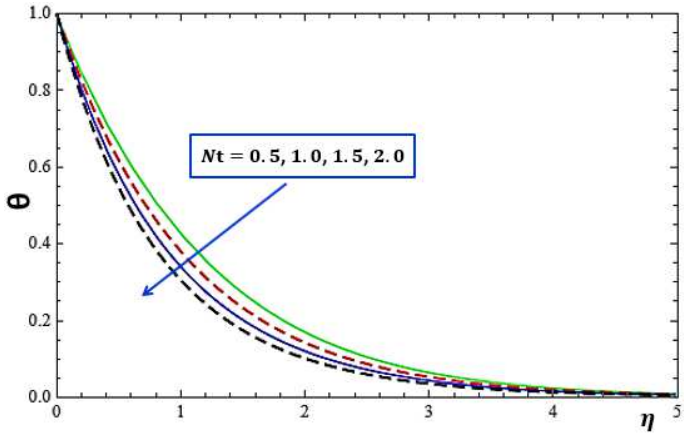


Fig. 12(a): Effect of thermophoresis parameter (Nt) on temperature profiles

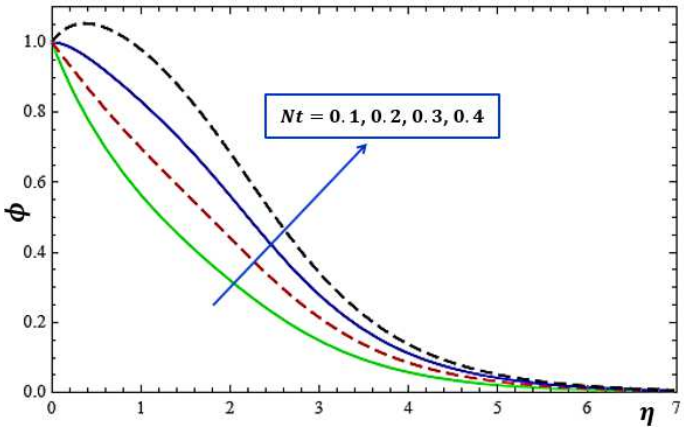


Fig. 12(b): Effect of thermophoresis parameter (Nt) on concentration profiles

In Figures 12(a) and 12(b), the effects of the thermophoresis parameter on the temperature and nanoparticle concentration profiles are shown, respectively. The process known as thermophoresis occurs when a fluid's temperature variation causes suspended particles to migrate, usually from hotter to cooler areas. In Figure 12(a), the temperature profiles noticeably decrease as Nt is increased. This is because particles are driven toward colder areas by the thermophoretic effect, which improves heat dissipation and decreases the thickness of the thermal boundary layer. In contrast, Figure 12(b) demonstrates that when Nt increases, the concentration profiles more pronouncedly rise. This is because the temperature difference causes particles to diffusively travel more readily, changing the concentration distribution within the domain. These results demonstrate thermophoresis's dual and important role in heat and mass transport processes by simultaneously suppressing local temperatures and enriching solutal concentration.

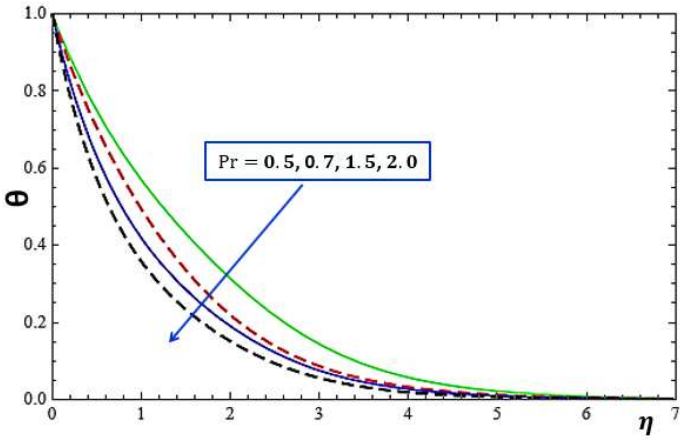


Fig. 13: Effect of Prandtl number (Pr) on temperature profiles

Figure 13 illustrates how the Prandtl number affects the temperature profiles. The relative efficiency of momentum transport against to heat transport in a fluid is described by the Prandtl number, which is the ratio of momentum diffusivity to thermal diffusivity. Our results indicate that the temperature profiles throughout the domain are significantly reduced when the Prandtl number is raised. This is because a fluid with a greater Pr has a lower thermal conductivity in relation to its viscosity, which leads to less thermal diffusion. The results shown here emphasize how the Prandtl number controls the behavior of the boundary layer and the efficiency of thermal transport in convective heat transfer systems.

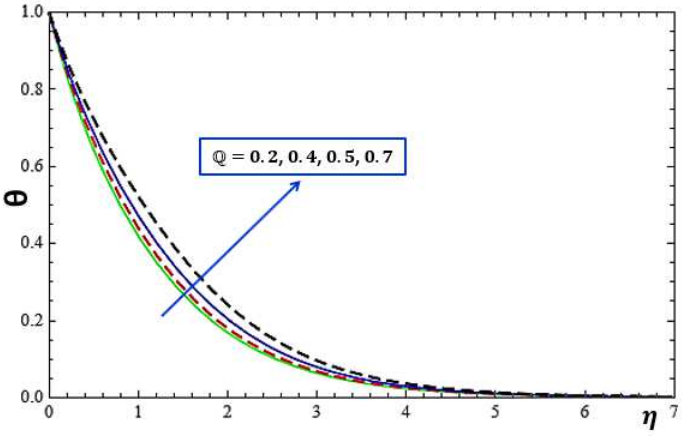


Fig. 14: Effect of heat source parameter ($\mathbb{Q}$) on temperature profiles

Figure 14 shows the impact of the heat source parameter on the temperature profiles. The heat source parameter describes how thermal energy is generated or absorbed internally inside the medium. Throughout the domain, the temperature profiles are markedly higher as the heat source parameter rises. The reason for this increase is that increased heat generation raises the fluid's internal energy, which leads to increased thermal diffusion. The trend shows that increased internal heat generation intensifies convective and conductive heat transfer processes by

thickening the thermal boundary layer. This result emphasizes how important localized heat sources are for regulating thermal behavior and system energy transmission.

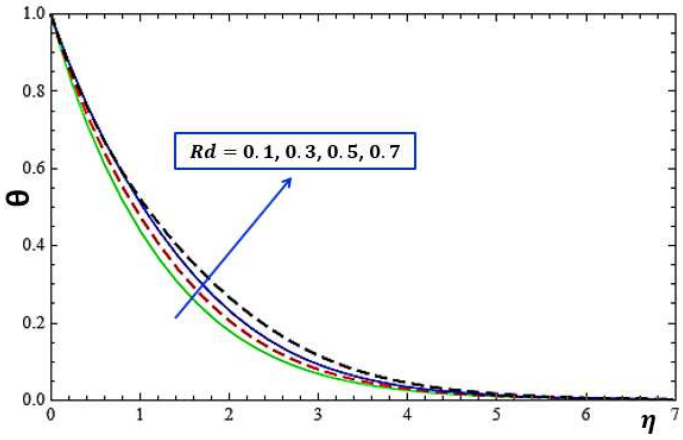


Fig. 15: Effect of radiation parameter (Rd) on temperature profiles

Figure 15 depicts the impact of the radiation parameter on temperature profiles. The radiation parameter measures how much heat transfer occurs inside the medium as a result of thermal radiation. It is evident from the figure that the temperature profiles ascend over the boundary layer as the radiation parameter escalates. This pattern is explained by the fact that a greater release of heat energy into the fluid is caused by higher values of the radiation parameter. The fluid's thermal state is improved by this extra heat, which raises its temperature noticeably. As a result, increasing the radiation parameter causes the thermal boundary layer to thicken, signifying that thermal energy further expands into the fluid. This emphasizes how important thermal radiation is for enhancing the system's total heat transmission.

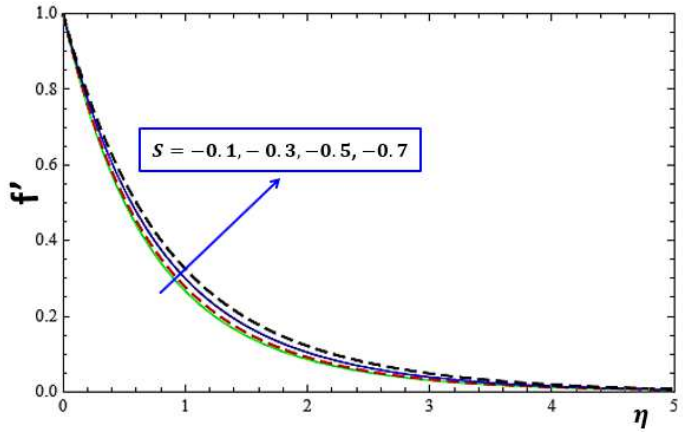


Fig. 16(a): Effect of injection parameter (S) on velocity profiles

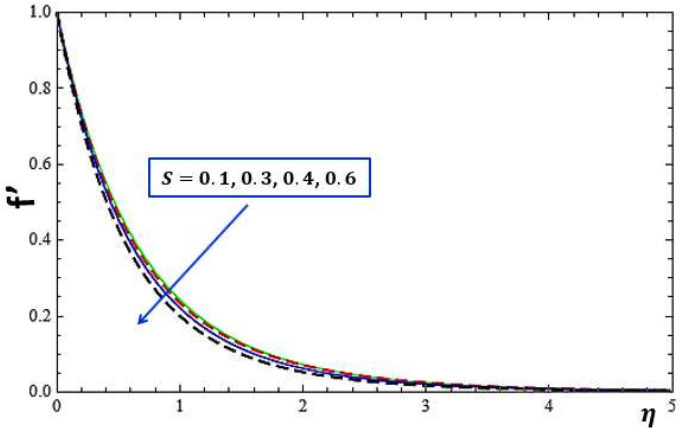


Fig. 16(b): Effect of suction parameter (S) on velocity profiles

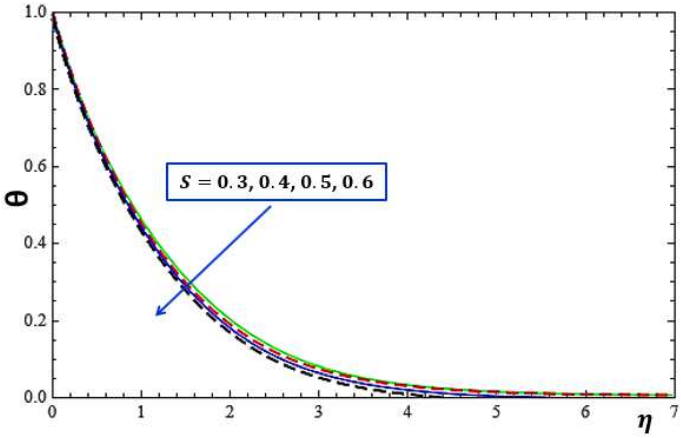


Fig. 16(c): Effect of suction parameter (S) on temperature profiles

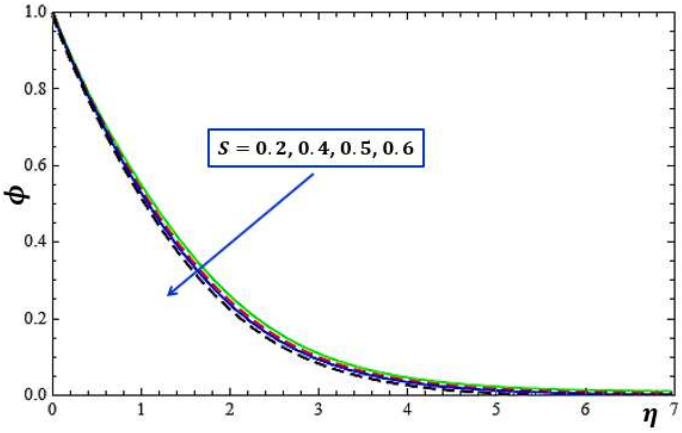


Fig. 16(d): Effect of suction parameter (S) on concentration profiles

In Figure 16(a) through 16(d), the impact of the mass transfer parameter on the dimensionless velocity, temperature and concentration profiles is illustrated. Figure 16(a) shows how the velocity profile is affected by the injection parameter ($S < 0$). It has been shown that the fluid velocity inside the boundary layer rises relatively and the

momentum boundary layer deepens accordingly as the injection parameter gets more negative (for example, from -0.1 to -0.7). The reason for these phenomena is because the fluid injection from the surface provides additional momentum to the boundary layer, which effectively boosts and intensifies the flow. On the other hand, Figures 16(b), 16(c) and 16(d) show how the suction parameter ($S > 0$) affects the temperature, concentration and velocity profiles, respectively. In each of the three figures, the corresponding profiles slightly decrease as the suction parameter increases. Physically, this behavior is described because the decelerated fluid particles close to the wall are removed by suction at the porous surface. As a result of this action, the momentum, temperature and concentration boundary layers become thin and the corresponding profiles decrease as the flow is drawn closer to the surface. This emphasizes the essential role that injection and suction play in regulating the transport phenomena within a system.

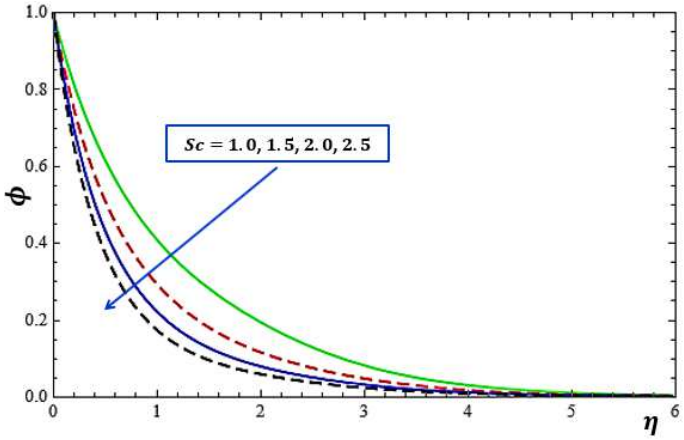


Fig. 17: Effect of Schmidt number (Sc) on concentration profiles

Figure 17 illustrates how Schmidt number affects concentration profiles. The Schmidt number signifies the ratio of momentum diffusivity to mass diffusivity, hence demonstrating the relative significance of viscous forces compared to molecular diffusion. As Sc grows, the mass diffusivity declines, which results in thinner concentration boundary layers. Consequently, concentration profiles are significantly lower throughout the flow area with greater Schmidt numbers. Larger Sc inhibit species diffusion, resulting in steeper gradients and a more pronounced concentration drop away from the surface, which causes this trend. The findings consistently demonstrate that raising Sc considerably reduces the species distribution, underscoring the crucial role that lowered mass diffusivity plays in controlling boundary layer transport phenomena.

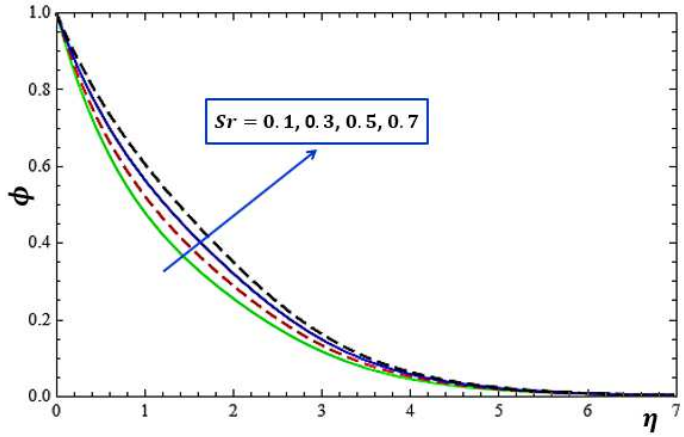


Fig. 18: Effect of Soret number (Sr) on concentration profiles

Figure 18 depicts the impact of the Soret number on the concentration profiles. A temperature gradient causing a mass flux is known as thermodiffusion, and its importance is characterized by the Soret number. As the Soret number rises, it indicates that thermally-driven mass transport is becoming more prevalent than normal molecular diffusion. Accordingly, a significant increase in the species concentration is seen throughout the domain when the Soret number is raised. The reason for this trend is that with higher temperature gradients, particles migrate more intensely from hotter to cooler regions. The findings consistently show that the concentration boundary layer widens significantly with increasing Soret number, highlighting the crucial role that this number plays in controlling mass transfer processes in thermosolutal convection systems.

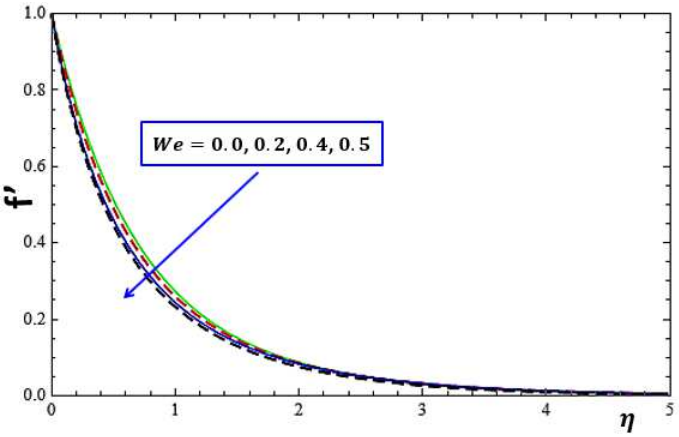


Fig. 19: Effect of Weissenberg number (We) on velocity profiles

Figure 19 shows the impact of the Weissenberg number on the velocity profiles. In a viscoelastic fluid, the We is an essential parameter that determines the relative dominance of elastic forces over viscous forces. The velocity profiles show a slight decrease throughout the domain as We rises. This diminution is outlined by the predominance of elastic forces, which prevent deformation and inhibit the fluid's forward motion. The trend shows that thinner

momentum boundary layers are produced when the velocity gradient close to the boundary is inhibited by the elastic stresses. Hence, the rise in We highlights the importance of elasticity in regulating rheological behavior and transport phenomena in non-Newtonian fluids by acting as a constraint on convective transport and modifying the flow structure.

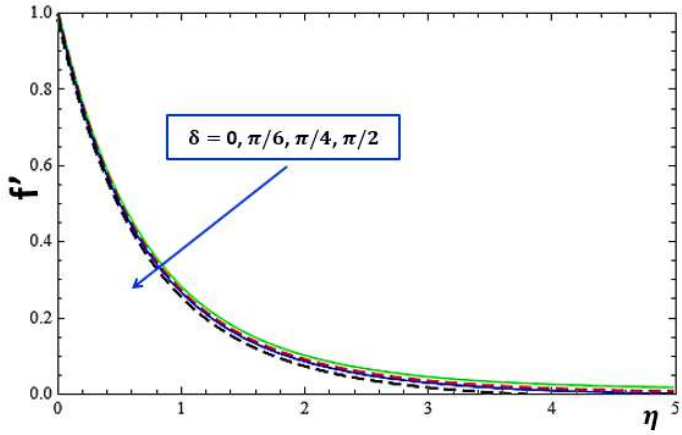


Fig. 20(a): Effect of angle of inclination (δ) of the magnetic field on velocity profiles

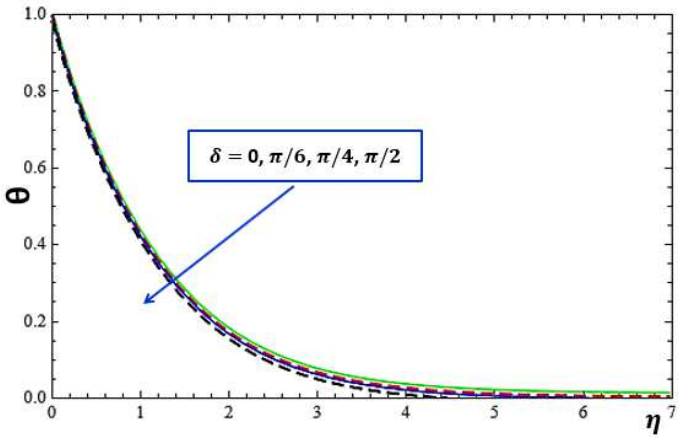


Fig. 20(b): Effect of angle of inclination (δ) of the magnetic field on temperature profiles

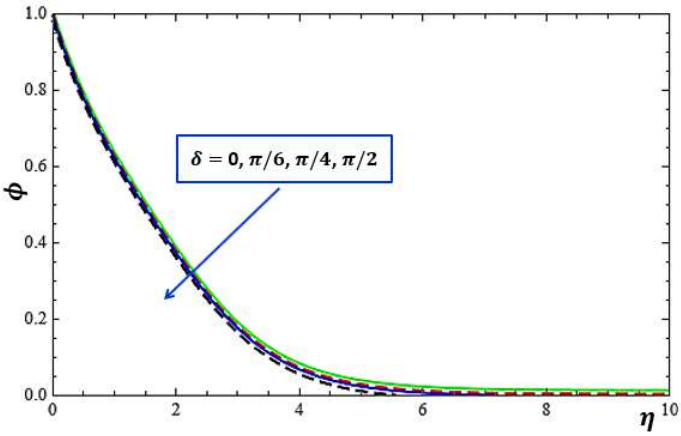


Fig. 20(c): Effect of angle of inclination (δ) of the magnetic field on concentration profiles

In Figures 20(a)–20(c), the impact of angle of inclination of the magnetic field on temperature, velocity and concentration profiles is illustrated. In MHD flows, the magnetic field's angle of inclination is important because it affects the direction and effective intensity of the Lorentz force acting on the fluid. This force that results from the interaction of the moving electrically conducting fluid with the magnetic field has a direct effect on the system's mass, momentum and energy transfer. As can be seen in Figure 20(a), the velocity profiles are suppressed slightly as δ increases. This diminution is caused by the increased magnetic field component that opposes fluid motion, which increases the Lorentz force and decreases momentum transport. The temperature profiles in Figure 20(b) likewise slightly decline as α increases. This diminishing pattern results because stronger magnetic resistance hinders fluid flow rate and then inhibits convective heat transfer, leading to a thinner thermal boundary layer. In a similar manner, concentration profiles, as depicted in Figure 20(c), exhibit a modest reduction as δ elevates. This is explained by the fact that the inclined magnetic field suppresses convective diffusion, which lowers solute transport and shrinks the concentration boundary layer. These findings together demonstrate the critical role of the angle of inclination of the magnetic field in reducing the transport phenomena, with a consistent decrease in temperature, velocity and concentration profiles as a result of heightened Lorentz forces, reduced convective heat transfer and constrained species diffusion.

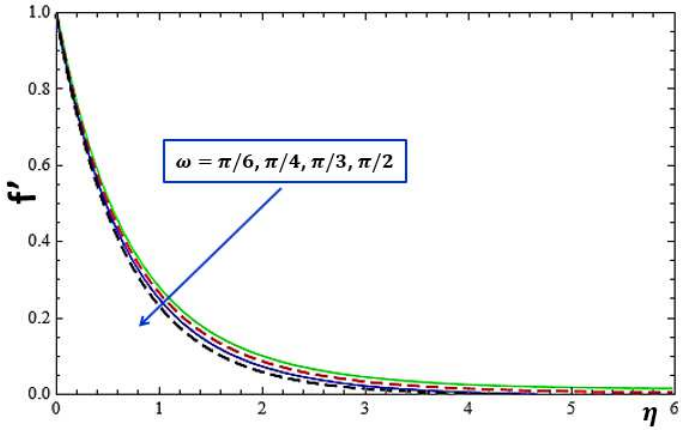


Fig. 21: Effect of angle of inclination (β) of the stretching sheet on velocity profiles

Figure 21 shows how the stretching sheet's angle of inclination affects the fluid flow's velocity profiles. Momentum transmission and shear stress distribution throughout the boundary layer are affected by the angle of inclination, which determines the stretching surface's orientation with respect to the flow direction. There is a discernible decrease in velocity profiles along the flow domain as the angle of inclination advances. This pattern results from the strengthened gravitational force that acts over the inclined surface, which elevates the shear forces and fluid motion resistance. Consequently, the inclination angle has a significant role in regulating the fluid dynamics and transport phenomena in the system, as evidenced by the subsequent reduction in the thickness of the momentum boundary layer.

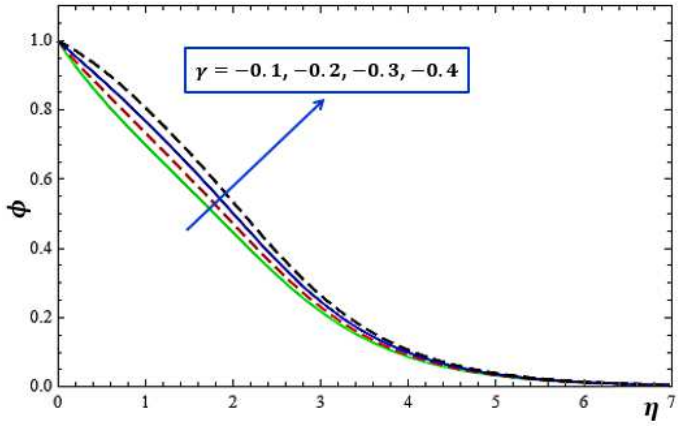


Fig. 22(a): Effect of chemical reaction parameter (γ) on concentration profiles

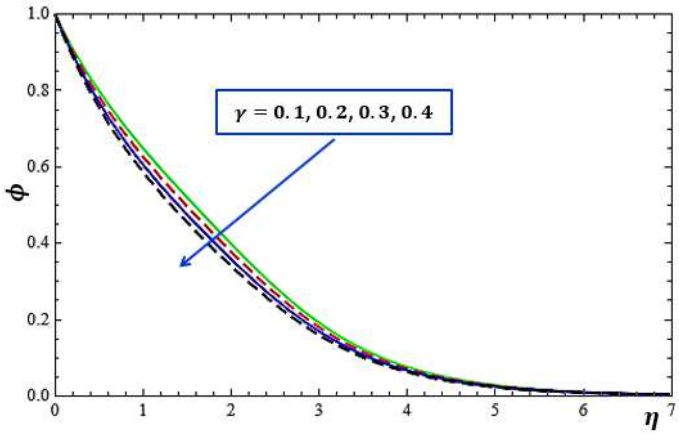


Fig. 22(b): Effect of chemical reaction parameter (γ) on concentration profiles

Figures 22(a)–(b) show the impact of the chemical reaction parameter on concentration profiles for both positive and negative values. The rate and nature of species transformation within the fluid domain are governed by the chemical reaction parameter, which has a major effect on the concentration distribution. The concentration profiles noticeably rise as γ gets more negative, suggesting either a generative response that promotes species accumulation or a decreased reaction rate. Conversely, the concentration profiles substantially drop as γ rises, indicating a faster consumption of reactive species as a result of a greater reaction rate. These patterns underscored the significance of the chemical reaction parameter in regulating species transport and the consequent concentration boundary layer thickness in the system.

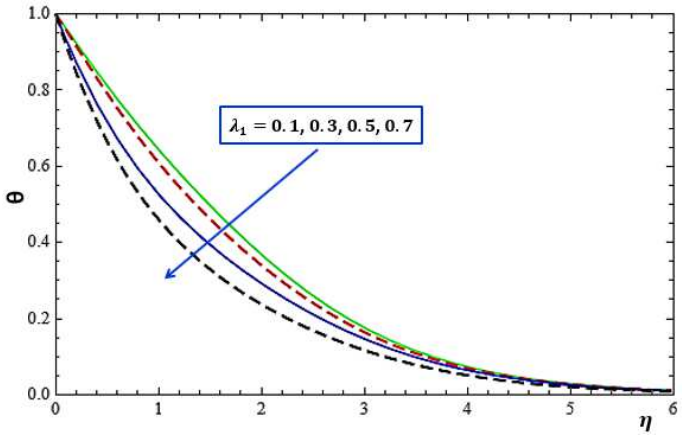


Fig. 23: Effect of relaxation time of heat flux (λ_1) on temperature profiles

The effect of the heat flow relaxation time on temperature profiles is illustrated in Figure 23. This parameter introduces hyperbolic wave-like heat propagation in place of the parabolic diffusion seen in traditional Fourier's law, quantifying the time lag between the heat flux and the temperature gradient. The temperature profiles across the thermal boundary layer show a noticeable decrease as λ_1 rises. Larger relaxation times induce an enhanced lag between the temperature gradient and the heat flux, which is caused by the non-Fourier heat conduction behavior. The temperature inside the domain drops as a result of this delay since it reduces the instantaneous thermal diffusion. This combined behavior emphasizes how λ_1 plays a crucial role in regulating thermal transport in advanced heat conduction circumstances by highlighting the non-local and finite-speed aspects of heat transfer under relaxation effects.

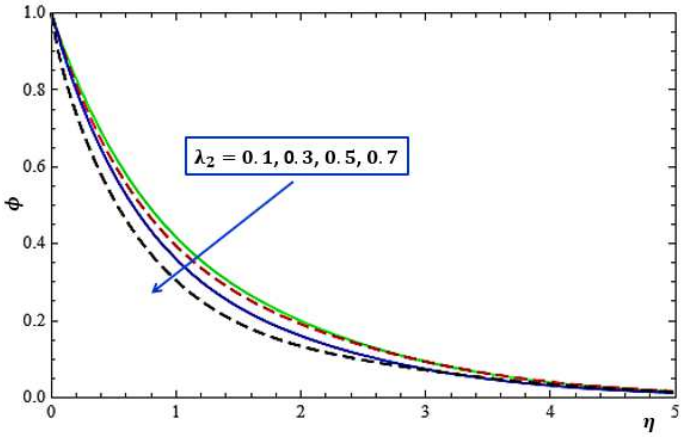


Fig. 24: Effect of relaxation time of mass flux (λ_2) on concentration profiles

Figure 24 shows how concentration profiles are affected by the relaxation time of mass flux. This parameter accounts for memory effects in solute transport by providing finite-speed diffusive waves that deviates from classical parabolic diffusion toward hyperbolic propagation, thereby reflecting the temporal lag in mass flow

response to concentration gradients within the Cattaneo-Christov framework. As the value of λ_2 increases, a significant decrease in concentration profiles is seen throughout the flow domain. This phenomenon is caused by the increased relaxation effect, which lowers the effective diffusivity and speeds up the solute concentration decay away from the surface because of decreased mass transport efficiency. These patterns demonstrate how the parameter plays a crucial role in non-Fickian mass dynamics, especially in viscoelastic fluids and systems when the fluid's relaxation time and the characteristic time scale of mass transfer are notably comparable.

Table 3: Impact of specific physical parameters on the skin-friction coefficient, Nusselt and Sherwood numbers, computed for $A = 0.3$, $Kp = 1.6$, $Sc = 1.2$, $Pr = 3.0$, $Nt = 0.4$, $Ec = 0.5$, $S = -0.01$, $Du = 0.5$, $Sr = 0.8$, $Gr_C = 0.6$, $\delta = \pi/12$ and $\mathbb{Q} = 0.1$.

We	M	Rd	γ	Nb	Gr_T	JH	ω	λ_1	λ_2	$-f''(0)$	$-\theta'(0)$	$-\phi'(0)$
0.0										1.370117	0.9257323	0.5100373
0.1										1.436380	0.8641872	0.5351922
0.2										1.524793	0.8279974	0.5407163
0.3	0.3									1.683141	0.8066836	0.5569746
	0.4									1.698513	0.8050761	0.5273419
	0.6									1.747559	0.8004485	0.5266628
	1.0	0.1								2.180639	0.7326772	0.5257746
		0.2								2.183396	0.6979709	0.5473518
		0.5								2.187114	0.6305773	0.7482110
		0.7	0.2							2.196995	0.5967810	0.8839070
			0.5							2.203070	0.5989327	1.1998540
			0.7							2.205745	0.6001512	1.2187390
			1.2	0.1						2.209480	0.6027495	1.3198850
				0.5						2.228648	0.5427204	1.7450290
				0.6						2.238393	0.5213410	1.7560270
				0.7	0.1					2.241392	0.3397984	1.8757550
					0.2					2.164359	0.3627760	1.9432760
					0.3					2.097374	0.3846202	2.0213970
					0.4	0.5				1.815783	0.3976916	2.0389181
						0.6				1.818521	0.3852247	1.6899060
						0.7				1.821176	0.3727241	1.6747410
						0.8	$\pi/6$			1.693509	0.3748186	1.6681240
							$\pi/8$			1.692923	0.3770124	1.6534240
							$\pi/10$			1.645726	0.3802205	1.6400240
							$\pi/12$	0.1		1.630551	0.4730260	1.6356450
								0.2		1.622614	0.4897613	1.6289840
								0.3		1.615437	0.5091419	1.6124650
								0.4	0.1	1.559352	0.5508979	1.5917620
									0.2	1.523283	0.5628311	1.6055240
									0.3	1.473946	0.5830684	1.6914650
									0.4	1.449445	0.6110839	1.9800220

The findings in Table 3 show that the skin-friction coefficient rises significantly with the Weissenberg number and the magnetic parameter, which reflects the Lorentz force and the strengthening of elastic stresses, both of which increase the velocity gradient near the wall. As We grows from 0.0 to 0.3, $-f''(0)$ increases quantitatively by about 23%, whereas an increase in M from 0.3 to 1.0 results in an augmentation of around 29.6%. In contrast, as increased thermal buoyancy increases the primary flow rate and decreases the near-wall velocity gradient, the skin-friction coefficient falls with the thermal Grashof number; for instance, an increase in Gr_T from 0.1 to 0.4 results in a drop of about 19%. The remaining parameters have quite little effects: Nb and JH cause slight increases of roughly 3% and 6.7%, respectively, whereas γ and Rd produce only marginal enhancements (approximately 0.5% and 0.7%). Conversely, ω, λ_1 and λ_2 reduce $-f''(0)$ by around 3.7%, 4.4%, and 7.1%, respectively. All of these results demonstrate that We and M have most substantial effects on wall shear, while other components have rather minor effects.

The Nusselt number decreases by roughly 13% as the Weissenberg number rises due to viscoelastic behavior thickening the thermal boundary layer. Because the Lorentz force slows the flow, a greater magnetic value further reduces heat transmission (~9% reduction). Because radiative heat transport tends to equalize temperatures and diminish conductivity gradients near the wall, thermal radiation results in a larger decline (~19%). Because of increased nanoparticle-driven micro-mixing in the boundary layer, the Brownian motion parameter has the most profound effect and lowers the heat-transfer rate by about 44%. Additionally, Joule heating reduces $-\theta'(0)$ (~6%) by acting as an internal heat source. The chemical reaction parameter, on the other hand, exhibits a minor positive influence (~1% increase), which is probably related to endothermic reaction processes that intensify surface heat gradients. Stronger buoyant forces increase heat transmission by approximately 17% as the thermal Grashof number rises. Geometric optimization encourages more effective thermal transport, as evidenced by the approximately 26% increase in $-\theta'(0)$ when the stretching-surface inclination angle is reduced from $\pi/6$ to $\pi/12$. Heat exchange is additionally strengthened by non-classical transport mechanisms: an increase in λ_1 results in a 16.5% increase in the Nusselt number and an additional 10.9% enhancement due to the intensification of concentration and temperature gradients under non-Fourier and non-Fickian effects.

The Sherwood number rises with the strength of mechanisms that improve fluid motion, thermal–mass coupling or microscale mixing. Mass transfer is facilitated by increased fluid stretching and relaxation, modified thermal fields that enhance mass diffusion, destructive chemical processes that sharpen concentration gradients ($\gamma > 0$) and micro-mixing caused by nanoparticles. Non-Fourier mass-flux relaxation and buoyancy forces produced by temperature differences offer further, yet modest, assistance. The Sherwood number rises by almost 68% when Rd is increased from 0.1 to 0.7. Rd has the greatest quantitative influence among these. Increases in We (0.0–0.3), Nb (0.1–0.7) and Gr_T (0.1–0.4) result in improvements of 9.2%, 42% and 9%, respectively, whereas an increase in γ from 0.2 to 1.2

produces a 49% increase. The impact of λ_2 is still remarkably significant, estimated to be 24%. On the other hand, the Sherwood number is decreased by characteristics that hinder the thermo-solutal coupling or inhibit the flow. A greater inclination angle shifts buoyancy forces away from the direction that promotes mass transfer; a longer heat-flux relaxation time delays the thermal response, thereby weakening mass diffusion; Joule heating transforms electrical energy into heat, lowering concentration gradients and a stronger magnetic field increases the Lorentz force, which resists fluid motion. Quantitatively, the Sherwood number decreases by around 6% when M is increased from 0.3 to 1.0, 18% when JH is increased from 0.5 to 0.8, 2% when ω is increased from π/6 to π/12 and a 3% decrease when λ_1 is increased from 0.1 to 0.4.

Conclusion

In this study, the unsteady flow of a Williamson nanofluid over a permeable, inclined stretching sheet was investigated using a thorough magnetohydrodynamic (MHD) analysis. The Cattaneo-Christov double-diffusion model was used in the study to take into consideration the relaxation of non-Fickian mass flux and non-Fourier heat. The flow controlling PDEs were transformed into a system of nonlinear ODEs using suitable similarity transformations. The semi-analytical OHAM was then used to solve these equations. The effects of significant physical parameters on velocity, temperature and concentration profiles, as well as surface drag and transfer rates, were critically examined.

The important results of this study are essentially summarized as follows.

Flow dynamics: Increases in the Weissenberg number, porosity parameter and unsteadiness parameter all considerably lower the fluid velocity. In particular, fluid motion is suppressed when a transverse magnetic field is applied because it creates a resistive Lorentz force. Moreover, a decrease in gravitational driving forces and an increase in magnetic resistance cause the flow to slow down as the inclination angles of the stretched sheet and the magnetic field are increased. In contrast, injection and greater thermal and solutal buoyant forces (Grashof numbers) increase the velocity profiles.

Thermal characteristics: As the radiation parameter, Eckert number, Joule heating and heat source parameter increase, more thermal energy is introduced into the system, which causes the fluid temperature to rise noticeably. A larger thermal boundary layer is also a result of Brownian motion and the diffusion-thermo (Dufour) effect. However, the Prandtl number and the unsteadiness parameter reduce the temperature distribution. Thermal inertia causes the thermal relaxation time parameter to behave in a special way, lowering the temperature in the near-field region while raising it in the far-field.

Mass transport: Thermophoresis, generative chemical processes and the Soret effect all improve the concentration profiles of nanoparticles. In contrast, the unsteadiness parameter, destructive chemical processes and the Schmidt number thin the concentration boundary layer. The mass flux relaxation time exhibits non-Fickian features, much like the thermal field, with longer relaxation times resulting in an accumulation of species concentration in the outer flow regime.

Engineering quantities

Skin-friction: Due to increased elastic pressures and Lorentz forces, wall shear is primarily affected by the Weissenberg number and the magnetic parameter, which increase the skin-friction coefficient by roughly 23% and 29.6%, respectively. On the other hand, wall shear is suppressed by thermal buoyancy; a rise in the thermal Grashof number causes a roughly 19% decrease.

Nusselt number: Brownian motion reduces the heat-transfer rate by about 44%, which is the most significant reduction. On the other hand, thermal transport is improved by geometric and buoyancy effects - the heat-transfer rate is increased by approximately 26% when the sheet's inclination angle is reduced from $\pi/6$ to $\pi/12$ and an additional improvement of approximately 17% is provided by a higher thermal Grashof number.

Sherwood number: Thermal radiation is the primary driver of the mass transfer rate and increasing the radiation parameter from 0.1 to 0.7 results in an increase of almost 68%. Furthermore, the Sherwood number increases by 49% when the chemical reaction parameter is increased, while mass transfer is inhibited by about 18% when Joule heating is increased from 0.5 to 0.8.

In conclusion, this work demonstrates that, in comparison with classical theories, the Cattaneo-Christov model offers a more accurate prediction of transport processes in viscoelastic nanofluids. The findings provide important information for improving industrial processes that include electromagnetic casting, high-temperature polymer extrusion and the thermal control of conductive nanofluids.

Future directions and prospects for model enhancement

Although the current study provides important insights, a number of improvements are required to more accurately reflect physical reality. **Ternary and hybrid nanofluids** should be the focus of future research in order to optimize thermal potential while taking **variable thermophysical parameters** into consideration. **Non-uniform porous** media settings and the **Darcy-Forchheimer model** should be combined to improve the flow media representation. For better accuracy in dynamic systems, **two-phase (Eulerian–Lagrangian) methods** and **3D vorticity-transport models** are recommended. **Particle aggregation and sedimentation** can be observed using these methods. Furthermore, electromagnetic analysis should be improved by adding **induced magnetic fields** and **Hall and ion-**

slip effects via generalized Ohm's law. Thermal analysis requires the incorporation of **multi-step reaction kinetics**, **spectrally resolved radiation** and **non-linear buoyancy** in high-temperature scenarios. Heat transport pathways should also be examined using the **entropy generation analysis**. Finally, the complexity of these proposed systems necessitates the use of **recently emerging advanced computational methods** to ensure the most accurate numerical solutions.

Declaration Statement

Author Contributions: Berihun Gizachew: Writing– original draft, Conceptualization. **Hunegnaw Dessie:** Formal analysis. **Eshetu Haile:** Supervision. **Tadesse Walelign:** Writing– review & editing.

Funding: The authors have not disclosed any funding.

Data of Availability: No data were used to support this study

Conflict of interest: All the authors declare that they have no conflict of interest.

Ethical Approval: Each of the authors discloses that this work was carried out in line with the acknowledged ethical research guidelines.

Consent for publication: All the authors agree with this manuscript's publication

References

[1] Williamson, R. V. (1929). The flow of pseudoplastic materials. *Industrial & Engineering Chemistry*, *21*(11), 1108-1111. https://doi.org/10.1021/ie50239a035

[2] Shateyi, S., & Muzara, H. (2020). On the numerical analysis of unsteady MHD boundary layer flow of Williamson fluid over a stretching sheet and heat and mass transfers. *Computation*, *8*(2), 55. https://doi.org/10.3390/computation8020055

[3] Abbas, A., Jeelani, M. B., Alnahdi, A. S., & Ilyas, A. (2022). MHD Williamson nanofluid fluid flow and heat transfer past a non-linear stretching sheet implanted in a porous medium: effects of heat generation and viscous dissipation. *Processes*, *10*(6), 1221. https://doi.org/10.3390/pr10061221

[4] Muzara, H., & Shateyi, S. (2023). Magnetohydrodynamics Williamson nanofluid flow over an exponentially stretching surface with a chemical reaction and thermal radiation. *Mathematics*, *11*(12), 2740. https://doi.org/10.3390/math11122740

[5] Geetha, R., Reddappa, B., Tarakaramu, N., Rushi Kumar, B., & Ijaz Khan, M. (2024). Effect of double stratification on MHD Williamson boundary layer flow and heat transfer across a shrinking/stretching sheet immersed in a porous medium. *International journal of chemical engineering*, *2024*(1), 9983489. https://doi.org/10.1155/2024/9983489

[6] Kumar, R., Mehta, R., Bhatnagar, A., Ozsahin, I., Uzun, B., Almohsen, B., & Ahmad, H. (2025). Numerical study of Williamson fluid flow over a stretching sheet with Newtonian heating embedded in a porous medium in presence of thermal radiation and heat source/sink. *Journal of Nonlinear Mathematical Physics*, *32*(1), 4. https://doi.org/10.1007/s44198-024-00258-1

[7] Choi, S. U. (1995). Enhancing thermal conductivity of fluids with nanoparticles. In *ASME international mechanical engineering congress and exposition* (Vol. 17421, pp. 99-105). American Society of Mechanical Engineers. https://doi.org/10.1115/IMECE1995-0926

[8] Buongiorno, J. (2006). "Convective Transport in Nanofluids." ASME. *J. Heat Transfer*. March 2006; 128(3): 240–250. https://doi.org/10.1115/1.2150834

[9] Ahmed, K., & Akbar, T. (2021). Numerical investigation of magnetohydrodynamics Williamson nanofluid flow over an exponentially stretching surface. *Advances in Mechanical Engineering*, *13*(5), 16878140211019875. https://doi.org/10.1177/16878140211019875

[10] Buzuzi, G., Magodora, M., Kudinha, M. T., Manamela, W. T., & Mambo, M. H. (2024). Steady MHD Williamson nanofluid flow past an inclined stretching sheet in the presence of heat generation, chemical reaction and aligned magnetic field. *IAENG International Journal of Applied Mathematics*. https://www.iaeng.org/IJAM/issues_v54/issue_6/IJAM_54_6_15.pdf

[11] Sankari, M. S., Rao, M. E., Shams, Z. E., Algarni, S., Sharif, M. N., Alqahtani, T., ... & Irshad, K. (2024). Williamson MHD nanofluid flow via a porous exponentially stretching sheet with bioconvective fluxes. *Case Studies in Thermal Engineering*, *59*, 104453. https://doi.org/10.1016/j.csite.2024.104453

[12] Arif, K., Saeed, S. T., Aslam, M. N., Younis, J., Riaz, A., & Saleem, S. (2025). Modelling cross-diffusion in MHD Williamson nanofluid flow over a nonlinear stretching surface via Morlet wavelet neural networks. *Scientific Reports*, *15*(1), 27287. https://doi.org/10.1038/s41598-025-06912-y

[13] Rao, A. S., Rao, P. P. B., & Ganteda, C. K. (2020). Magnetohydrodynamic Williamson fluid motion over an exponentially stretching sheet with chemically radiative heat source effects under suction/injection. *J. Math. Comput. Sci.*, *10*(6), 2634-2657. https://doi.org/10.28919/jmcs/4961

[14] Divya, G. P., Reddy, G. R., & Bindu, P. (2023). Unsteady MHD Casson and Williamson nanofluids over a permeable stretching sheet in the presence of thermal radiation and chemical reaction. In *1st international conference on essence of mathematics and engineering applications: ICEMEA 2021* (Vol. 2707, No. 1, p. 030005). AIP Publishing LLC. https://doi.org/10.1063/5.0143359

[15] Kumar, R. M., Raju, R. S., Mebarek-Oudina, F., Kumar, M. A., & Narla, V. K. (2024). Cross-diffusion effects on an MHD Williamson nanofluid flow past a nonlinear stretching sheet immersed in a permeable medium. *Frontiers in Heat and Mass Transfer*, *22*(1), 15-34. https://doi.org/10.32604/fhmt.2024.048045

[16] Sujatha, V., & Sridhar, W. (2025). Heat and mass transfer of MHD Williamson fluid flow past a shrinking/stretching sheet with dual stratification, radiation, Joule heating effect. *Journal of Naval Architecture and Marine Engineering*, *22*(1), 49-61. https://www.banglajol.info/index.php/JNAME/article/view/76875

[17] Darcy, H. (1856). *Les fontaines publiques de Dijon*. https://gallica.bnf.fr/ark:/12148/bpt6k624312/f1n657.pdf

[18] Alrihieli, H., Areshi, M., Alali, E., & Megahed, A. M. (2022). MHD dissipative Williamson nanofluid flow with chemical reaction due to a slippery elastic sheet which was contained within a porous medium. *Micromachines*, *13*(11), 1879. https://doi.org/10.3390/mi13111879

[19] Khader, M. M., Babatin, M. M., & Megahed, A. M. (2023). Numerical simulation by using the spectral collocation method for Williamson nanofluid flow over an exponentially stretching sheet with slip velocity. *Journal of Nonlinear Mathematical Physics*, *30*(3), 1134-1152. https://doi.org/10.1007/s44198-023-00115-7

[20] Prithvi, S., Vidya Shree, R., & Patil Mallikarjun, B. (2025). Analyzing MHD Williamson Fluid Over A Porous Stretching Sheet with Heat and Mass Transfer by Applying the Chebyshev Wavelet

Operational Matrix Method. *International Journal of Applied and Computational Mathematics*, *11*(2), 53. https://doi.org/10.1007/s40819-025-01838-5

[21] Aroloye, S. J. (2025). Impacts of thermal radiation, heat absorption and heat generation on the flow of hydro-magnetized Williamson fluid embedded in a porous medium. *Irish International Journal of Engineering and Applied Sciences*, *9*(2), 30-44. https://aspjournals.org/Journals/index.php/iijeas/article/view/1073?utm_source=chatgpt.com

[22] Cattaneo, C. (1948). Sulla conduzione del calore. *Atti Sem. Mat. Fis. Univ. Modena*, *3*, 83-101.

[23] Christov, C. I. (2009). On frame indifferent formulation of the Maxwell–Cattaneo model of finite-speed heat conduction. *Mechanics research communications*, *36*(4), 481-486. https://doi.org/10.1016/j.mechrescom.2008.11.003

[24] Khan, M. I., Alzahrani, F., Hobiny, A., & Ali, Z. (2020). Modeling of Cattaneo-Christov double diffusions (CCDD) in Williamson nanomaterial slip flow subject to porous medium. *Journal of Materials Research and Technology*, *9*(3), 6172-6177. https://doi.org/10.1016/j.jmrt.2020.04.019

[25] Abbas, W., Megahed, A. M., Morsy, O. M., Ibrahim, M. A., & Said, A. A. (2022). Dissipative Williamson fluid flow with double diffusive Cattaneo-Christov model due to a slippery stretching sheet embedded in a porous medium. *AIMS Math*, *7*(12), 20781-20796. https://doi.org/10.3934/math.20221139

[26] Salahuddin, T., Iqbal, M. A., Bano, A., Awais, M., & Muhammad, S. (2023). Cattaneo-Christov heat and mass transmission of dissipated Williamson fluid with double stratification. *Alexandria Engineering Journal*, *80*, 553-558. https://doi.org/10.1016/j.aej.2023.09.012

[27] Salahuddin, T., & Awais, M. (2024). Thermal and solutal transport by Cattaneo-Christov model for the magnetohydrodynamic Williamson fluid with joule heating and heat source/sink. *Heliyon*, *10*(7). https://doi.org/10.1016/j.heliyon.2024.e29228

[28] Malleswari, K., Nath, J. M., Reddy, M. V., Mala, M. S., & Dey, B. (2025). Thermal Performance of Cattaneo-Christov Heat Flux in MHD Radiative Flow of Williamson Nanofluid Containing Motile Microorganisms and Arrhenius Activation Energy. *Journal of Computational and Theoretical Transport*, *54*(1), 45-67. https://doi.org/10.1080/23324309.2024.2419007

[29] Gizachew, B., Dessie, H., Haile, E., & Walelign, T. (2025). Investigation of Time-Dependent MHD Flow Characteristics of Williamson Nanofluid across a Heated, Permeable and Inclined Stretching Sheet within a Porous Medium. *Physics Open*, 100349. https://www.sciencedirect.com/science/article/pii/S2666032625000997

[30] Shah, Z., O. Alzahrani, E., Dawar, A., Alghamdi, W., & Zaka Ullah, M. (2020). Entropy generation in MHD second-grade nanofluid thin film flow containing CNTs with Cattaneo-Christov heat flux

model past an unsteady stretching sheet. *Applied Sciences*, *10*(8), 2720. https://doi.org/10.3390/app10082720

[31] Liao, S. J. (1992). On the proposed homotopy analysis technique for nonlinear problems and its applications. *Shanghai Jiao Tong University*.

[32] Liao, S. (2012). *Homotopy analysis method in nonlinear differential equations* (Vol. 153). Beijing: Higher education press. https://doi.org/10.1007/978-3-642-25132-0

[33] Vajravelu, K., & Van Gorder, R. (2013). *Nonlinear flow phenomena and homotopy analysis* (Vol. 2). Berlin: Springer. https://doi.org/10.1007/978-3-642-25132-0

[34] Liao, S. (Ed.). (2013). *Advances in the homotopy analysis method*. World Scientific. https://doi.org/10.1142/8939

[35] Shamshuddin, M. D., Mabood, F., & Salawu, S. O. (2021). Flow of three-dimensional radiative Williamson fluid over an inclined stretching sheet with Hall current and nth-order chemical reaction. *Heat Transfer*, *50*(6), 5400-5417. https://doi.org/10.1002/htj.22130

[36] Mukhopadhyay, S. (2013). MHD boundary layer slip flow along a stretching cylinder. *Ain Shams Engineering Journal*, *4*(2), 317-324. https://doi.org/10.1016/j.asej.2012.07.003

[37] Mabood, F., Lorenzini, G., Pochai, N., & Ibrahim, S. M. (2016). Effects of prescribed heat flux and transpiration on MHD axisymmetric flow impinging on stretching cylinder. *Continuum Mechanics and Thermodynamics*, *28*(6), 1925-1932. https://doi.org/10.1007/s00161-016-0519-9